DEVELOPMENT OF AN AIRBORNE POLLUTION MEASUREMENT SYSTEM

by

Tyson David Graehl

A thesis submitted to the faculty of
The University of Utah
in partial fulfillment of the requirements for the degree of

Master of Science

Department of Mechanical Engineering

The University of Utah

December 2011

The University of Utah Graduate School

STATEMENT OF THESIS APPROVAL

The thesis of **Tyson David Graehl**

has been approved by the following supervisory committee members:

Meredith Metzger	, Chair	**11/15/2011** Date Approved
Robert Stoll	, Member	**11/15/2011** Date Approved
Kuan Chen	, Member	**11/15/2011** Date Approved

and by **Timothy Ameel**, Chair of the Department of **Mechanical Engineering**

and by Charles A. Wight, Dean of The Graduate School.

ABSTRACT

The Sky-scan Atmospheric Monitoring Instrument (SAMI) consists of a low profile, autonomous unmanned aerial vehicle (UAV) that provides a platform for remotely sampling airborne contaminants in real-time over large distances. In this manner, the SAMI may be used to acquire pollutant concentration at various altitudes, relevant, for example, to smokestack emissions, and in high-risk locations where conditions hazardous to humans may exist. The SAMI system employs an innovative miniaturized pollution measurement device that captures discrete gas samples at programmed intervals during flight and records the corresponding pollutant concentration using an on-board data logger. The pollution measurement device integrates seamlessly with the body of the UAV and directly interfaces with the autopilot hardware/software. The pollution measurement device draws/expels gas into/out of the sampling chamber by taking advantage of the pressure drop that naturally occurs over the surface of the aircraft. This eliminates the need for an external pump, thereby affording significant weight and cost savings. The present thesis documents the response characteristics of the SAMI system and demonstrates the functionality of the system for the specific pollutant carbon monoxide (CO). The potential application is real-time monitoring of air pollution dispersion due to automobile traffic.

CONTENTS

LIST OF FIGURES

NOMENCLATURE

α	kinetic energy coefficient
μ	fluid dynamic viscosity
ρ	fluid density
τ	time lag
c	chord length
c_a	molar concentration of air
C	gas concentration
C_0	initial concentration
$C_{cal,1}$	lower calibration CO concentration
$C_{cal,2}$	upper calibration CO concentration
C_g	source gas concentration
C_p	pressure coefficient
D	tube diameter
e	tube roughness
f	friction factor
f_0	initial friction factor guess
g	acceleration of gravity
h_l	majors losses
h_{l_T}	total head loss
h_{l_m}	minor losses
J	percentage change in sensor output due to a temperature difference
K	magnitude of step input
K_l	loss coefficient
L	length of pipe
p_∞	pitot tube static pressure
$p_{\infty,0}$	pitot tube stagnation pressure
P	ambient pressure
P_1	inlet fluid pressure
P_2	outlet fluid pressure
P_{cal}	barometric pressure as measured during calibration
R^*	universal gas constant
Q_g	source gas volumetric flow rate
Q_{za}	zero-air volumetric flow rate
r	the consumption rate
R	gas constant for air

R^*	universal gas constant
Re	Reynolds number
t	time
T	ambient temperature
T_{cal}	ambient temperature as measured during calibration
$\bar{V}$	average fluid velocity
V_{ADC}	CO sensor voltage as measured by the autopilot ADC
$V_{cal,1}$	sensor output voltage corresponding to $C_{cal,1}$
$V_{cal,2}$	sensor output voltage corresponding to $C_{cal,2}$
V_{sensor}	CO sensor output voltage
Vol	internal volume of the pollution measurement device
z	height

ACKNOWLEDGEMENTS

Partial funding for this project was provided by the National Science Foundation. I want to express my gratitude to my advisor, Prof. Meredith Metzger, for the knowledge and guidance that she provided during this project. Also, thanks to Erik Van Zwol, whose help with the design and manufacturing of the electronic circuit board for the pollution measurement device was crucial to the completion of this design. I would also like to thank my parents for their encouragement and support. Finally, a very special thanks to my wife, Lindsay, for her patience, love and sacrifice throughout the duration of this project.

CHAPTER 1

INTRODUCTION

Traditionally, pollution monitoring has been limited to permanent ground stations. The measurements obtained at ground-based measurement stations are generally limited to ground level pollution. In order to overcome the limitations of ground stations, various types of manned aircraft have been used to obtain accurate pollution levels at different altitudes (Corrigan *et al.*, 2008; Patterson *et al.*, 2005). A variety of measurement devices have been mounted on these aircraft. They can carry measurement and monitoring equipment capable of measuring gas concentration levels and particle count, monitoring atmospheric conditions, and conducting aerial surveillance. In many cases, pollution measurement equipment requires a great deal of space and can be very heavy. The missions to collect data using manned aircraft have been limited by the endurance levels of the crew and the risk to human life. These manned flights can also be very expensive due to fuel costs which increase with the increased weight of the instrumentation. Recent developments in the aerospace industry have provided researchers with an alternative to manned aircraft.

In recent decades, unmanned aerial vehicles (UAVs) have become very useful instrument platforms in the military, law enforcement, and scientific communities. They are used for applications such as surveillance, combat support, communications, pollution monitoring, and atmospheric condition monitoring. Use of UAVs allows for smaller, lighter aircraft that require less fuel and less space for launch and retrieval. UAVs can have very high endurance limits and can reach remote or even dangerous areas to make measurements. However, small UAVs have a lower load carrying capacity than their manned counterparts. Therefore, any measurement equipment must be small, light weight, and low power. The present thesis

describes the Sky-Scan Atmospheric Monitoring Instrument (SAMI) along with a new, miniaturized pollution measurement device designed to overcome the limitations of heavier pollution monitoring equipment. The SAMI is a lightweight autonomous UAV (AUAV) capable of flying along a predetermined path while monitoring temperature, pressure, airspeed, and pollution levels while recording the exact global positioning system (GPS) location.

The pollution measurement device is a generic design and is intended to be adaptable for use with a variety of sensors. For the purposes of the present thesis, the chosen sensor detects carbon monoxide (CO) concentrations. However, a variety of small sensors are readily available for detecting other pollutants such as carbon dioxide (CO_2), hydrogen sulfide (H_2S), nitrogen dioxide (NO_2), ozone (O_3), and sulfur dioxide (SO_2). The device could easily be altered to accommodate a different sensor. CO is a byproduct of incomplete combustion and can be very hazardous to human health. Sources include internal combustion engines, fossil fuel burning power plants, fireplaces, and wildfires. CO could easily exceed EPA limits during inversions when pollutants remain trapped in the air near the surface of the earth (Nev, 2011). CO was the chosen pollutant for multiple reasons. First, the selected sensor was relatively inexpensive and readily available. Also, the tanks of CO used during calibration and testing were inexpensive. Finally, the concentrations used during testing were low enough that some exposure to the gas did not pose a significant risk to the operator.

CO is of particular interest to multiple government agencies concerned with the health of the public. The United States (US) Environmental Protection Agency (EPA) requires that states monitor the ambient CO concentration levels to ensure that they remain under the acceptable limit as outlined in the National Ambient Air Quality Standards (NAAQS) (2011). The US Department of Energy (DOE) regulates CO emissions from fossil fuel burning power plants (2011). The SAMI system could be used to monitor the CO levels around and above sources of CO such as high automobile traffic areas and around fossil fuel power plants. It could also be used in determining how the CO is transported and how it disperses.

1.1 Literature Review

While the concept of using UAVs to monitor pollution levels is not new, miniature measurement instruments are still in the process of being developed. Many research projects have been devoted to the use of both small and large UAVs for this task. The following are summaries of articles of research projects of a similar nature.

The *Bidule UAV* (Wong, 2001) was developed by researchers at the University of Sydney. The Bidule, which is considered a miniature air vehicle (mAV), was developed in order to test the design and flight capabilities of a concept before designing a micro air vehicle (μAV). One of the goals of this mAV was to outfit the aircraft with a small camera as well as a "micro" payload, such as a CO sensor. The Bidule would be able to access remote or potentially hazardous locations in order to obtain measurements (Spoerry & Wong, 2001).

At the Scripps Institution of Oceanography in San Diego research has been performed using a fleet of AUAVs (Corrigan *et al.*, 2008). The AUAVs were used to monitor pollutants such as aerosols and black carbon. The goal of the study was to obtain a vertical profile of aerosols and black carbon more accurately than existing ground stations. The majority of the measurement devices used were miniaturized versions of existing instruments as well as newly designed miniature instruments. Scripps was able to develop an aerosol absorption photometer that was much smaller than the original rack mounted unit. The new aerosol absorption photometer allowed the Scripps team to utilize a much smaller AUAV.

The *Aerosonde Robotic Aircraft* (Holland *et al.*, 2001) is a UAV developed by Aerosonde Pty Ltd based in Melbourne, Australia and was developed as a main component in an unmanned aircraft system (UAS). The aircraft was designed to be operated from anywhere in the world, as well as to operate autonomously. The Aerosonde aircraft has a range of more than 3000 km and an endurance of more than 30 $hours$. It was originally used to gather meteorological data and has proven to be a robust system. Future developments include the addition of interchangeable instrument payloads. The planned instrumentation includes equipment capable of detecting CO, CO_2, O_3, and SO_2.

The *Pegasus UAV* (Everaerts *et al.*, 2004) is in the process of being developed by the Flemish Institute for Technological Research. The Pegasus aircraft will be capable of flying at altitudes of $12 - 20\ km$ carrying a number of measurement instruments. The Pegasus will be capable of taking infrared, thermal, and visual images as well as be able to collect Light Detection and Ranging (LIDAR), Synthetic Aperture Radar (SAR), and atmospheric data. Atmospheric data will include temperature and measurements of methane, nitrogen oxides, CO, CO_2, O_3, and water vapor. The UAV will be quite large, having a wingspan of $15 - 20\ m$, as well as have the ability to remain aloft for long periods of time. The Pegasus will be powered by solar energy collected by solar panels mounted to the top of each wing which will allow the aircraft to sustain flights as long as 7 *months*. The Pegasus will be autonomous and will be capable of transmitting the data it collects to ground-based command stations.

The *AirRobot AR100* (Bartholmai & Neumann, 2010) microdrone was developed by AirRobot GmbH & Co. KG company in conjunction with the German Federal Institute for Materials Research and Testing. The aircraft is a quadrocopter (consisting of four rotors) that is controlled remotely by an operator. Due to the small size ($1\ m$ diameter) and hover capability of the aircraft, it is well suited to enter areas where space is limited. The endurance of the aircraft is limited to 30 *minutes* and the range is limited to $1\ km$. The aircraft is fitted with a multigas detector capable of identifying five separate gases. A variety of interchangeable sensors may be used to detect gases such as ammonia (NH_3), CO, CO_2, H_2S, NO_2, oxygen (O_2), and SO_2. Algorithms were in the process of being developed to aid the aircraft in tracking plumes of a target gas. The aircraft was successfully tested in an enclosed chamber as well as in the field.

The *ACR Silver Fox* (Patterson *et al.*, 2005) UAV was used in 2004 to remotely monitor the eruption of Mount St. Helens in Washington. Manned aircraft were used to monitor the volcano both before and during the eruption. However, the flights were limited due to the risk posed to human life aboard the aircraft. The 2004 eruption was viewed as an opportune time to test the feasibility of using UAVs to monitor various aspects of the volcano. The aircraft was fitted with regular and IR cameras used to

view activity within the crater of the volcano, a location very hazardous for human missions. A sensor suite consisting of seven sensors was available for use. However, the sensors were not used due to the fact that the expected gas concentrations exceeded the range of the sensors as well as the moderately long response time ($30-60$ *seconds*) of the sensors.

1.2 US Patent Search

In order to identify existing pollution measuring devices, a patent search was conducted. The search was limited to devices that had the ability to be mounted on a UAV. However, the patent search was not limited to devices that measure CO, but also included various types of pollutants such as CO_2 and O_3. These patents are listed in Table 1.1.

The *apparatus for sensing hydrocarbons and carbon monoxide* (Logothetis & Soltis, 1993) was developed by researchers at the Ford Motor Company for detecting hydrocarbons and CO in the exhaust of a motor vehicle. The device utilizes resistor-type

Table 1.1. Reviewed patents

Issue Date	**Patent Number**	**U.S. Patent Title**	**Inventor Name(s)**
10/05/1993	5250169	Apparatus for sensing hydrocarbons and carbon monoxide	Logothetis et al.
12/25/2007	7312452	Mobile remote detection device and remote detection method for methane gas accumulations	Klingenberg, et al.
08/11/2009	7573573	Method and particle measuring and counting apparatus with selectable channels of a specimen flow	Yufa
06/29/2010	7746240	Sensing system and components for detecting and remotely monitoring carbon monoxide in a space of concern	Vij
02/08/2011	7884937	Airborne tunable mid-IR laser gas-correlation sensor	Prasad, et al.

or calorimetric-type sensors capable of detecting hydrocarbons and CO. The types of sensors intended to be used in this application tend to be more accurate in the presence of oxygen. However, the intended mounting location for the device is in the exhaust line of a motor vehicle which may have very low levels of oxygen due to the air-to-fuel ratio used. To overcome this low-oxygen condition, the device utilizes a set of electrodes on opposite sides of a solid electrolyte to produce a specific amount of oxygen. The device allows the measurement gas to enter the device through an aperture and the produced oxygen to enter through another aperture. The voltage across the sensor is used to determine the hydrocarbon and CO levels in the exhaust.

The *mobile remote detection device and remote detection method for methane gas accumulations* (Klingenberg *et al.*, 2007) is a small, low weight, and low power method of detecting methane gas. The detection device consists of a light source, backscattered light detector, and a device to facilitate evaluation. The light emitted from the light source is emitted in two types of pulses. The first pulse of light is tuned to the same wavelength as the methane spectral signature and is absorbed by the methane gas particles. The second is a reference light pulse with a different frequency. The overlap area illuminated by the unabsorbed light and by the reference light is measured by the backscattered light detector. These data are used to determine methane gas levels. The detection device is intended to be a mobile device, capable of being mounted on a vehicle such as an aircraft.

A *method and particle measuring and counting apparatus with selectable channels of a specimen flow* (Yufa, 2009) was designed to measure particle size as well as count particles in a given flow. The apparatus can be used to measure and count particles of gases and liquids. The flow enters through a single inlet line where the flow rate is measured. The flow then comes to a valving system. The valving system is used to select which size of particle, and therefore which type of particle, is to be measured. Exiting the valving system is a set of lines. Each line contains a filter used to filter the flow such that only certain particles are allowed to pass. All of the lines converge after the filters such that there is only one outlet from the valving/filter system. When a single valve is open, the gas or liquid only flows through a single filter and

then exits through the outlet. Once the flow leaves the filtration system it enters the measurement device. In the measurement device, a light/laser beam is directed through the flow to a detection device. The detection device measures the scattered light to determine the number of particles of a given size in the flow. Following the detection device the flow passes through a pumping device intended to draw the flow through the entire system.

A *sensing system and components for detecting and remotely monitoring carbon monoxide in a space of concern* (Vij, 2010) was designed to monitor CO levels in a given space such as an aircraft cabin, a garage, or a shop. A detection device uses a CO sensor mounted inside of a housing. Air is drawn into the housing using a fan. Both the temperature and pressure inside of the housing are monitored using a temperature probe and pressure sensor. If the temperature falls below a predetermined value a heating element is turned on to ensure that the measuring device maintains a certain level of performance. An on-board microprocessor takes the reading from the pressure sensor and modifies the output signal in order to compensate for the effects due to pressure change. The measurement system is linked to a monitoring device which is used to display the current CO levels reported by the detection device. The monitoring device can also be used to reset the detection device and retest the CO level.

The *airborne tunable mid-IR laser gas-correlation sensor* (Prasad *et al.*, 2011) uses a tunable laser as well as a series of mirrors and infrared (IR) detectors to determine the presence and/or concentration of a target gas. The laser beam is directed out into a portion of the atmosphere and the reflected beam is captured in the device. The reflected beam is split and passes through multiple chambers containing gases. One portion of the beam passes through a chamber that contains a reference sample of air that does not contain the target gas. The other beam portions pass through other chambers containing varying levels of the target gas. A detector on the side of the chamber opposite from the beam entrance point is used to detect the transmitted signals. These are then used to determine concentration levels of the target gas. The detection unit is intended to be mounted on a mobile platform such as a vehicle or

aircraft in order to obtain remote measurements.

1.3 New Contribution

The present thesis describes the development of a new, innovative pollution measurement device. The present device is unique as it was designed to capture an air sample from which to take a pollution measurement. The device is intended to overcome the sensor output delay due to extended sensor response times by isolating a static sample. This limits the spacial resolution of the measurements based on the response time within the device; however, it increases the accuracy of the measurement by allowing the output of the sensor to stabilize. Also, the low profile and low power requirements of the device allow it to be easily mounted on a small UAV.

The design of the measurement device is intended to be generic such that it can be easily adapted to accommodate a variety of gas sensors. For the purposes of the present thesis as CO sensor was used. The manufacturer of the sensor also manufactures a sensor of identical size that detects H_2S and would be easily used in the same device. A range of small sensors that function using the same principles as the present sensor are readily available, as previously described. The device design can be modified to accommodate the different sensor dimensions while still functioning based on the same principles of operation as the present design. The microprocessor is also easily programmable to allow for device closure time of varying lengths according the needs of a specific sensor.

1.4 Outline of Thesis

The SAMI system is an air pollution monitoring system that can quickly be deployed to remote areas. It contains a newly designed pollution measurement device that captures a static air sample and measures the concentration of the target gas in that sample. The sensor output is recorded along with the GPS location and altitude where the sample was captured. These data can be used to create a three-dimensional plot of the target gas concentration levels for a given area of interest.

The present thesis first presents the principle of operation of the SAMI system. Next, the design methodology used is described. Here the component descriptions and

design considerations are provided. Equations and results are discussed for the aircraft static pressure analysis, including both wind tunnel tests and numerical simulations. Bench-top test methods and results are presented which characterize the pollution measurement device in terms of the mechanical function, target gas consumption, response time, and a system transfer function. Finally, test results from preliminary test flights are presented.

CHAPTER 2

SAMI SYSTEM DESIGN

2.1 Principle of Operation

The SAMI pollution monitoring system is comprised of a pollution monitoring device mounted on a UAV as well as a ground-based control station, as shown in Figure 2.1. The UAV is controlled by an autopilot system which communicates with the control station wirelessly. As the aircraft flies along a predetermined path it encounters pollution. The pollution measurement device mounted on the aircraft takes advantage of the pressure differences created by the airfoil to force air to flow through it. During the flight the user, from the control station, commands the autopilot to record the desired data. At predetermined intervals the device's valves close, capturing an air sample from which to take a reading. At the time the valves close additional data are recorded such as position, altitude, atmospheric pressure,

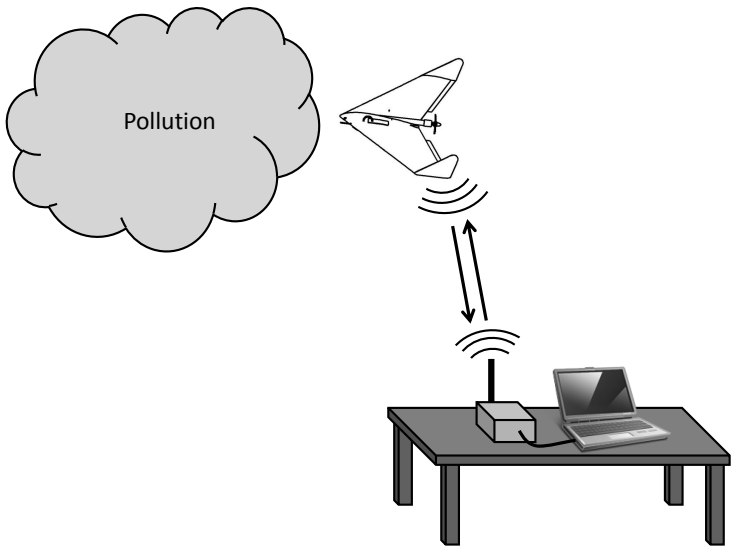

Figure 2.1. Diagram of the basic principle of operation of the SAMI System.

and air temperature. After the device has had sufficient time to accurately measure the concentration of the pollutant the valves open, releasing the previous sample. This process is repeated until the available on-board memory is full, at which time the collected data are transmitted down to the command station computer. During the postprocessing phase, the collected pressure, temperature, and sensor readings are used to determine the concentration of the target pollutant at each sampled position and altitude.

2.2 Design Methodology

Detailed descriptions of the aircraft, autopilot system, and CO sensor used in the SAMI system design are provided below. Also described are the decisions made in designing the air sample capture device, used in conjunction with the CO sensor, as well as the design of the custom circuitry.

2.2.1 Aircraft Platform

The aircraft platform selected for the SAMI design was the *Unicorn* by Unicorn Ventures L.L.C. The Unicorn is a flying wing-type aircraft popular among model airplane hobbyists and is shown in Figure 2.2. Table 2.1 lists the specifications of the aircraft. The wing structure is made of expanded polypropylene (EPP) foam which provides an inexpensive, lightweight, and damage resistant structure. The structural integrity of the Unicorn platform is further increased by the use of carbon fiber spars. The aircraft is assembled using epoxy glue and fiber-reinforced tape, further increasing the structural strength and stiffness. The aircraft is able to withstand multiple impacts with minimal damage. When damage does occur, the EPP foam is easily repaired with fiber-reinforced tape and epoxy glue.

The Unicorn has only two control surfaces to control the aircraft during flight, whereas a conventional aircraft has four. Mounted along the trailing edge of each wing is an elevon. An elevon combines the functions of both the conventional aileron and elevator. Each elevon is controlled by a single servo motor. The aileron and elevator signals from the controller are mixed before they are sent to the servo motors. Also, the Unicorn does not have a traditional rudder. Instead, it has vertical stabilizers in

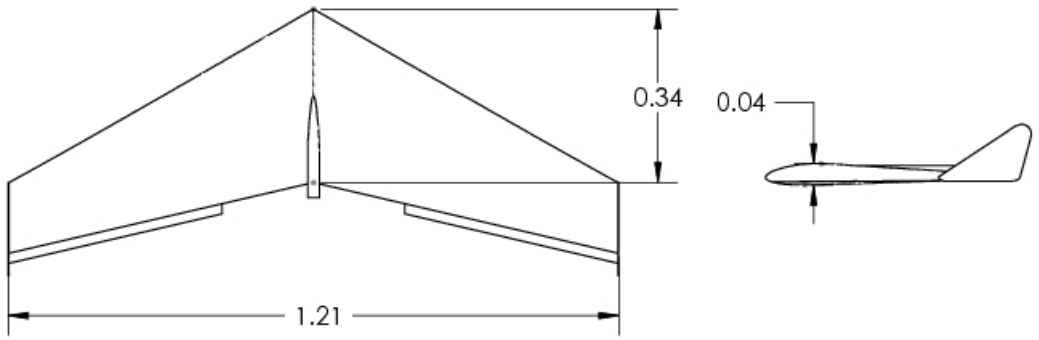

Figure 2.2. Diagram of the base Unicorn aircraft. The units are in m.

Table 2.1. Unicorn aircraft dimensions

Characteristic	Value
Wingspan*	1.21 m
Principle Chord Length	0.34 m
Maximum Thickness	0.04 m
Typical Cruising Speed	14 m/s
Wing Area*	0.35 m^2

* Source: http://unicornwings.stores.yahoo.net/specifications.html

the form of winglets at the end of each wing.

The aircraft is powered using a single 11.1 *volt*, 3-cell lithium polymer (LiPo) battery and is propelled by a brush-less electric motor. Brush-less motors are more efficient than regular electric motors due to the lack of brushes, which reduces the internal friction of the motor. The motor is mounted behind the center of the aircraft and pushes it forward rather than pulling. The propeller used is a pusher-type propeller to be used in conjunction with a pusher motor.

Due to the low-profile shape of the wing, the Unicorn has a higher lift to drag ratio than traditional aircraft and is, therefore, more efficient. The fuselage of a traditional aircraft increases drag while making little or no contribution to lift. The entire Unicorn aircraft, with the exception of the winglets and elevons, produces lift during flight. However, the aircraft is more difficult to control as there is no horizontal

stabilizer or rudder. For this reason it was advantageous to use an autopilot to control the aircraft during flight.

2.2.2 Autopilot System

The use of an autopilot is beneficial for multiple reasons. First, as stated above, flying wing aircraft can be relatively difficult to control manually. Second, an autopilot increases the range of operation of a remote controlled aircraft by allowing the aircraft to leave the visual range of the operator. Finally, the selected autopilot has on-board data acquisition (DAQ) capabilities, thus eliminating the need to utilize a separate DAQ.

The aircraft is controlled by the *Kestrel* autopilot system developed by Procerus Technologies. The Kestrel autopilot system is a commercial off-the-shelf (COTS) product. The system is comprised of the autopilot and associated avionics as well as the ground station equipment.

2.2.2.1 Autopilot and Associated Avionics

The autopilot and associated avionics are the components mounted to the aircraft that monitor and control its flight. The autopilot is a small circuit board that contains a processor, accelerometers, gyros, pressure sensors, servo ports, serial ports, an analog-to-digital (ADC) port, and a power port. Attached to one of the serial ports is a GPS sensor. The GPS receives positional data from satellites orbiting the earth and transmits that data to the autopilot. Those data are then used by the autopilot to guide the aircraft. The motor speed controller and two elevon servos connect to the servo ports where they receive signals from the autopilot in order to control the aircraft during flight. A modem and dipole antenna are also connected to the autopilot which allow the autopilot to transmit signals to and receive signals from the ground station. One pressure port is used to monitor the barometric pressure during flight. This aids with determining the altitude of the aircraft. This pressure sensor is also used in conjunction with the pressure port connected to the pitot tube by the autopilot to determine the airspeed of the aircraft. Figures 2.3 and 2.4 show mounting locations of the autopilot and associated avionics.

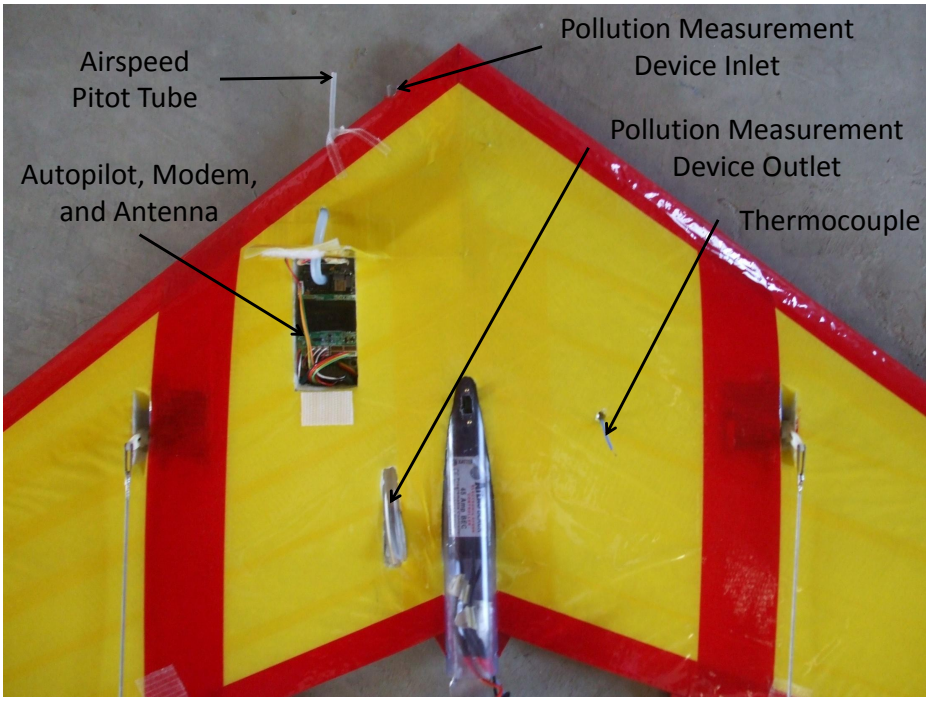

Figure 2.3. Top view of SAMI aircraft with components mounted.

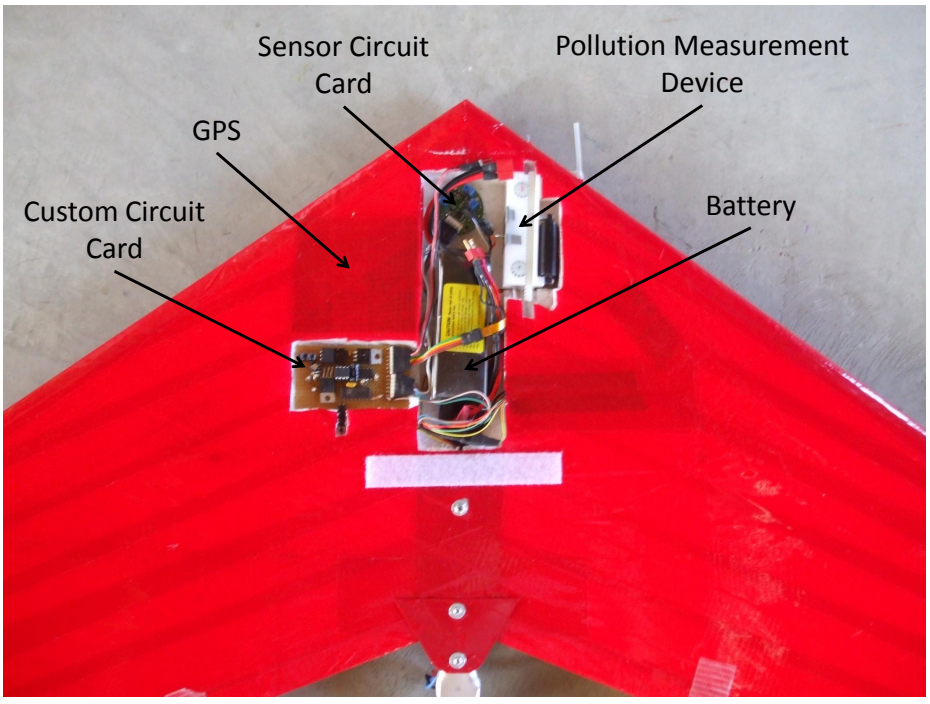

Figure 2.4. Bottom view of SAMI aircraft with components mounted.

2.2.2.2 Ground Station Components

The ground station components include a laptop, the Virtual Cockpit Software, the Commbox, and an RC transmitter. The Virtual Cockpit software is loaded onto the ground station computer. These components are shown in Figure 2.5. The Virtual Cockpit graphical user interface (GUI) provides the operator with a terminal used to designate waypoints and other flight plan settings and to upload the flight plan to the autopilot. The Virtual Cockpit is also used to control in-flight data logging, to monitor flight progress, and to monitor the aircraft's vitals such as battery voltage, airspeed, and communication strength. The Commbox enables communication between the autopilot and the ground station computer and is connected to the ground station computer via a RS232 serial cable fitted with a serial-to-USB converter. The Commbox has an external radio frequency (RF) antenna that extends the range of communication between the aircraft and the Commbox to approximately 10 km in optimal conditions. The Commbox also facilitates communication between the RC transmitter and the autopilot, used when manual flight control is desired.

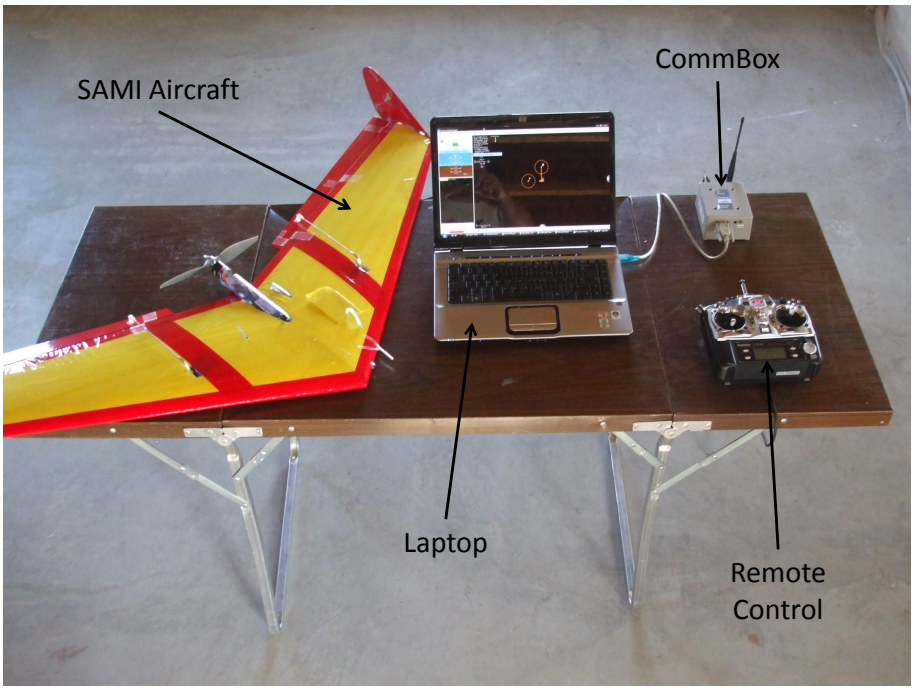

Figure 2.5. Photograph displaying the SAMI aircraft and the ground station components.

The Virtual Cockpit software is used by the operator to control the aircraft. Prior to a flight, the user obtains a satellite image of the flight area using Google Earth. This image, along with the positional data (latitude and longitude), is uploaded to the Virtual Cockpit. The image is saved and displayed when the aircraft is physically located near that area. Figure 2.6 shows the Virtual Cockpit with an image loaded. The lines and symbols on the image represent the flight plan as set by the user. The house symbol represents the location of the Ground Station. The aircraft symbol represents the location of the SAMI aircraft. The circle surrounding the letter "T" is the area to which the plane flies during take-off. Points 1-5 represent the waypoints that the aircraft follows during regular flight. The dashed circle surrounding the letter "R" is known as the rally zone. The plane flies to the rally zone in preparation for landing. When landing, the aircraft leaves the rally zone and follows the approach line until it reaches the landing point, represented by "L". During flight the actual flight path is recorded and displayed on the map as dots.

Figure 2.6. Example of a flight plan as set up in Virtual Cockpit.

2.2.3 Pollution Measurement Device

In order to monitor pollution levels during flight using the Unicorn airframe, a miniature pollution measurement device was designed. The present pollution measurement device is intended to be adaptable in order to utilize a variety of sensors. The principles of operation are the same for various types of gas sensors. For the purpose of the present thesis it was decided that a CO sensor would be used.

2.2.3.1 CO Sensor

The chosen CO sensor is part number 3ET1CO1500F made by KWJ Engineering, Inc and is shown in Figure 2.7. This sensor was chosen because of its small size, low cost, and for the wide range of CO concentrations it can detect. This CO sensor measures only 14.5 *mm* square yet can measure CO concentrations from 0-1500 *parts per million* (*ppm*) with an uncertainty of $\pm$ 5 *ppm*, depending on the circuitry. The sensor is an amperometric gas sensor which utilizes an electrochemical reaction to measure CO concentrations. The sensor consists of a working electrode, reference electrode, counter electrode, and a liquid electrolyte. The target gas diffuses through a porous membrane and oxidizes when it comes in contact with both the working electrode, located directly behind the membrane, and the electrolyte. As each molecule of CO oxidizes on the working electrode two electrons are released and

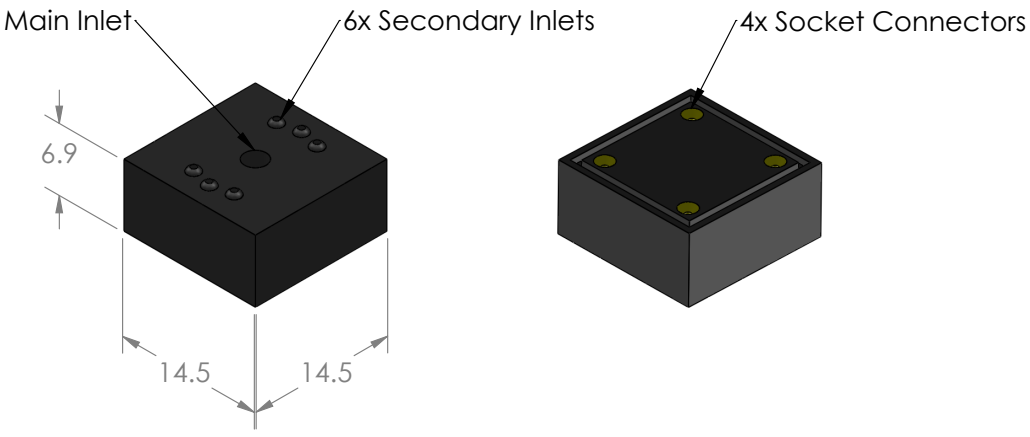

Figure 2.7. Schematic of the CO sensor. The units are in *mm*.

the byproduct is CO_2. The electrons released by the reaction flow from the working electrode to the external circuitry, a potentiostat. The counter electrode completes the circuit back to the electrolyte. The current created by the oxidation of CO is converted to a voltage by the potentiostat (KWJ, 2008).

The potentiostat consists of three potentiometers used to set the bias, offset, and gain. For this CO sensor the bias is set to zero. During calibration the sensor is saturated with zero air, which contains no CO, and the offset is adjusted until the output voltage reads zero. Finally, the sensor is saturated with air containing 200 *ppm* CO and the gain is adjusted until the output voltage is 3 *volts*. Per the recommendation of the manufacturer, when the gas is applied to the sensor during calibration the volumetric flow rate should be as low as possible. They stated that a volumetric flow rate of 0.2 standard liters per minute (SLM) was acceptable. Also, it was recommended that during calibration each concentration be applied to the sensor for a minimum of 25 *minutes* in order to allow the output of the sensor to stabilize (Patel, 2011). The output of the sensor is linear. Therefore this is the extent of the calibration. Using the linear relationship of the calibration, the values of any output voltage can be directly converted to a concentration. Following calibration, the same potentiostat is used during actual testing (KWJ, 2008).

The sensor is sensitive to changes in temperature and pressure. These changes affect the output of the sensor and thus, must be taken into account. The output of the sensor increases by 0.8% for each increase of $1°C$ from 0 to $22°C$ and 1% from 22 to $35°C$. With respect to pressure, the output of the sensor increases by 6 to 7% for each increase of 6895 Pa (Patel, 2011). The temperature and pressure at calibration serve as a base for determining the correct concentration of CO when the pressure and/or temperature change. A MATLAB function was created in order to compensate for temperature and pressure variations during data collection. The function uses the sensor output voltage, V_{out}, ambient temperature, T, and barometric pressure, P, measured during data collection along with the calibration information and percentages above, in conjunction with the following equation, to determine the actual concentration.

$$C = V_{sensor}\left(1 + J\left(T - T_{cal}\right)\right)\left(1 + 0.065\left(P - P_{cal}\right)\right)\left(\frac{C_{cal,2} - C_{cal,1}}{V_{cal,2} - V_{cal,1}}\right) \tag{2.1}$$

where T_{cal} and P_{cal} are the ambient temperature and barometric pressure readings, respectively, as measured during calibration, $C_{cal,1}$ is the lower calibration CO concentration, $C_{cal,2}$ is the upper calibration CO concentration, $V_{cal,1}$ is the sensor output voltage corresponding to $C_{cal,1}$, and $V_{cal,2}$ is the sensor output voltage corresponding to $C_{cal,2}$. J is the percentage change in the sensor output due to the temperature difference and is determined using the temperature-based percentages above.

H_2S also affects the sensor's readings. H_2S reacts with the sensor in a way similar to CO. Therefore, exposure to H_2S will cause the output of the sensor to be inaccurate. To overcome this problem the manufacturer added a chemical filter to the sensor. This filter effectively blocks the H_2S. However it does increase the response time of the sensor possibly by 100× or more. The sensor has a typical response time of less than 30 *seconds* (to reach 90% of the actual concentration) (KWJ, 2008). Therefore, the response time of the sensor may be as much as 50 *minutes*. However, the results of response time tests performed in the lab are discussed in more detail in Section 4.1.5.

As a result of the chemical reaction occurring in the sensor, molecules of CO are consumed. The consumption rate can be derived from the span of the output signal as defined by the manufacturer which is $70 \pm 15\ nA/PPM$. Implications of the consumption rate on the postprocessing of the raw data are discussed in Section 4.1.4.

According to the manufacturer of this sensor, the sensor does not perform well at high air flow rates. As this measurement device is intended to be mounted on an aircraft traveling at speeds ranging from $10 - 20\ m/s$, it was apparent that a housing would be required to capture an air sample from the flow in order to obtain an accurate CO concentration measurement (KWJ, 2008).

2.2.3.2 Air Sample Capture Device

In order to capture an air sample and hold it static during measurement, an air sample capture device was designed. It was important to design a device small enough

to fit in the Unicorn aircraft, which only measures approximately 38 mm thick at the point where the device would be located. As a result, the device shown in Figure 2.8 was designed.

The device housing is generally rectangular in shape and measures approximately 25.4 $mm \times 25.4\ mm \times 76.2\ mm$. It has a through hole that extends down the length of the housing from end to end. Along one of the sides is a cutout just large enough to accept the CO sensor. The cutout was designed such that all seven of the sensor's holes would be exposed to the flow with minimal flow blockage due to the sensor.

On either side of the sensor is a cylindrical valve. Mounted to the top of each valve is a pinion gear. The two pinion gears are linked together with a rack gear.

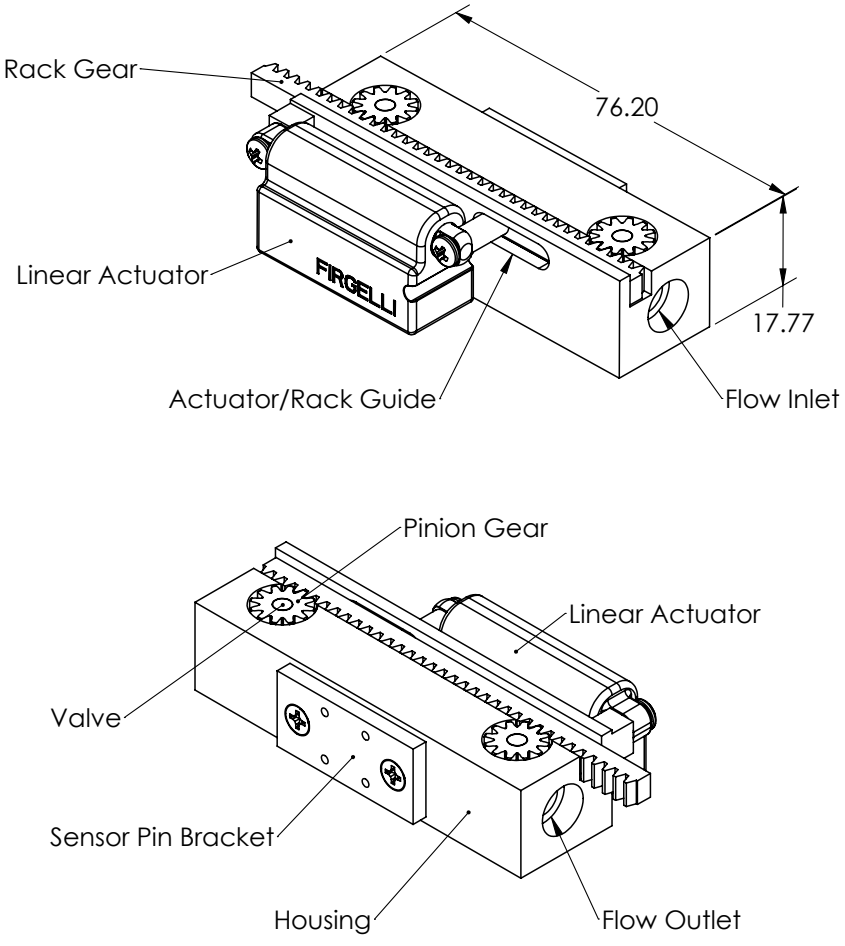

Figure 2.8. Schematic displaying the pollution measurement device and its components. Units are in mm.

The rack gear is connected to a linear actuator. As the actuator arm extends and retracts the valves open and close. The actuator is controlled by the microprocessor described in Section 2.2.3.3. Connected to each end of the device are vinyl tubes. The tube on one side conducts the air flow from the inlet on the aircraft to the inlet of the measurement device. The other tube serves as the outlet and conducts the air from the measurement device to the outlet on the aircraft.

The air sample capture device was designed such that the pressure difference created by the airfoil itself would be sufficient to drive air through the device, thus eliminating the need for a pump or fan. In order to reduce the pressure losses in the measurement device, a relatively constant cross-sectional area was maintained from the inlet to the outlet. The number and severity of bends in the tubing were also kept to a minimum.

In order to aid in the determination of an appropriate internal diameter, the flow of air through the tubing and device was analyzed. A mathematical model was created to model the flow through the measurement device. A derivation of equations that describe the mathematical model is outlined in the Appendix.

The resultant equations are,

$$0 = \left(\frac{P_1 - P_2}{\rho}\right) - \left[\left(\sqrt[0.5]{\frac{1}{-2.0 \log\left[\frac{e/D}{3.7} + \frac{2.51}{\left(\frac{\rho \bar{V} D}{\mu}\right) f_0^{0.5}}\right]}}\right) \frac{L}{D} + 0.5\right] \frac{\bar{V}^2}{2}, \tag{2.2}$$

and

$$f_0 = 0.25 \left(\log\left[\frac{e/D}{3.7} + \frac{5.74}{\left(\frac{\rho \bar{V} D}{\mu}\right)^{0.9}}\right]\right)^{-2}, \tag{2.3}$$

where f_0 is the initial friction factor guess, e is the tube roughness, D is the tube inner diameter, ρ is the fluid density, $\bar{V}$ is the average fluid velocity, μ is the fluid dynamic viscosity, P_1 is the inlet fluid pressure, and P_2 is the outlet fluid pressure.

When equation (2.3) is inserted into equation (2.2) the resulting equation represents the dynamic fluid model for the measurement device from the inlet to the outlet. $\bar{V}$, the average fluid velocity through the device, is needed to prove that the pressure difference between the inlet and the outlet is sufficient to overcome the pressure losses in the measurement device. To ensure that air flows through the device at a reasonable rate a value for D was chosen such that $\bar{V} >> 0$. The change in pressure between the inlet and the outlet, ΔP (or P_1 - P_2), was determined by the wind tunnel and CFD testing outlined in Chapter 3.

Commercially available tubing sizes were considered when selecting a value for the inner diameter of the device. The sizes considered are listed in Table 2.2. In order to maintain a constant cross-sectional area through the device, and thus reduce the pressure losses, the diameter of the through hole in the device matched the chosen tube diameter. The fluid properties used in the calculation were for air at atmospheric pressure and at a temperature of 20 °C. MATLAB was used to solve equations (2.2) and (2.3) simultaneously for $\bar{V}$ when provided with values for e, D, ρ, μ, and ΔP. Preliminary calculations suggested that the ΔP may be as high as 100 Pa. Therefore, $\bar{V}$ through the device was calculated for pressures of $15 - 100$ Pa using each of the tube inner diameters listed in Table 2.2. The results are shown in Figure 2.9.

Figure 2.9 shows that with the selected range of tube sizes and the expected ΔP values, the typical airspeed of the aircraft is not attainable within the device. It was also important to choose a tube with an outer diameter small enough to reasonably

Table 2.2. Tube size options.

Option	Inner Diameter (mm)	Outer Diameter (mm)
A	3.2	6.3
B	4.8	7.9
C	6.3	9.5
D	7.9	12.7

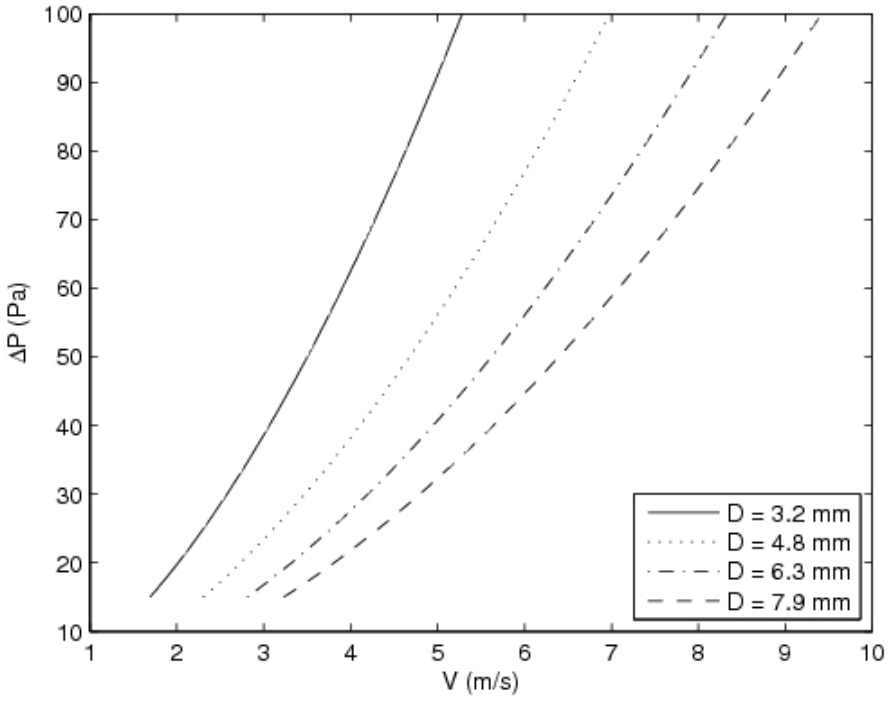

Figure 2.9. Plot of the average device air velocity for different tube sizes as a function of ΔP.

fit within the aircraft. It was decided that the outer diameter of the tubing should be no greater than 1/4 of the maximum thickness of the aircraft. This decision was made in order to avoid weakening the aircraft structure more than necessary since material would need to be removed from the aircraft. Thus, tube Option C was chosen as the outer diameter fit the aforementioned criteria. If ΔP were to reach 100 Pa the average air velocity through the device would be approximately 8.3 m/s, which corresponds to a volumetric flow rate of approximately 15.8 L/min.

2.2.3.3 Custom Control/Interface Circuitry

A custom circuit card was designed in order to control the linear actuator and to power the CO sensor. The custom circuit card provides an interface between the air sample capture device and the autopilot, regulates the battery power in order to appropriately power the CO sensor, and also monitors the temperature of the air flow. Table 2.3 lists the main components used on this custom circuit card and Figure 2.10 is a schematic showing how the circuit card is wired.

Electricity is supplied to the circuitry by the same battery used to power the autopilot and the electric motor. Although the specified battery voltage is 11.1 *volts*, a fully charged battery actually has a voltage of about 12.2 *volts*. As the battery charge is depleted during flight the voltage is reduced. One of the autopilot's fail-safes instructs the aircraft to return to the home base once the battery voltage reaches 10.5 *volts*. Therefore, the useful voltage range expected to be supplied to the control/interface circuitry is $10.5 - 12.2$ *volts*. As the SAMI is commanded to return to home base at 10.5 *volts*, all pollution testing will take place at voltages between 10.5 and 12.2 *volts*.

The voltage supplied to the control/interface circuitry is first regulated to 5 and 10 *volts*. The 10 *volt* regulator used is a low dropout (LDO) regulator with a dropout voltage of 0.3 *volts*. In order to guarantee 10 *volts* from this regulator a voltage greater than 10.3 *volts* must be supplied from the battery. This 10 *volt* regulator was chosen as 10.5 *volts* is the lowest voltage expected during operation. The 5 *volt* regulator has a maximum dropout voltage of 2.5 *volts*. Therefore, the minimum voltage supply needed for the 5 *volt* regulator is 7.5 *volts*, which is well below the lowest available voltage.

Table 2.3. Custom circuit card components.

Component	Description	Function
LM7805	5V Voltage Regulator	Regulates the source voltage down to 5V
BAJ0BC0T-ND	10V Voltage Regulator	Regulates the source voltage down to 10V
PIC12F683	8-Bit Microprocessor	Programmed to command the linear actuator to open and close at predetermined intervals
TLE 5206-2S	H-Bridge for DC Motors	Takes the open/close signals from the PIC and controls the DC motor in the linear actuator
AD595AQ	Thermocouple Amplifier	Amplifies the voltage created by the thermocouple
LM358	Op-Amp	Amplifies the voltage signal from the thermocouple amplifier

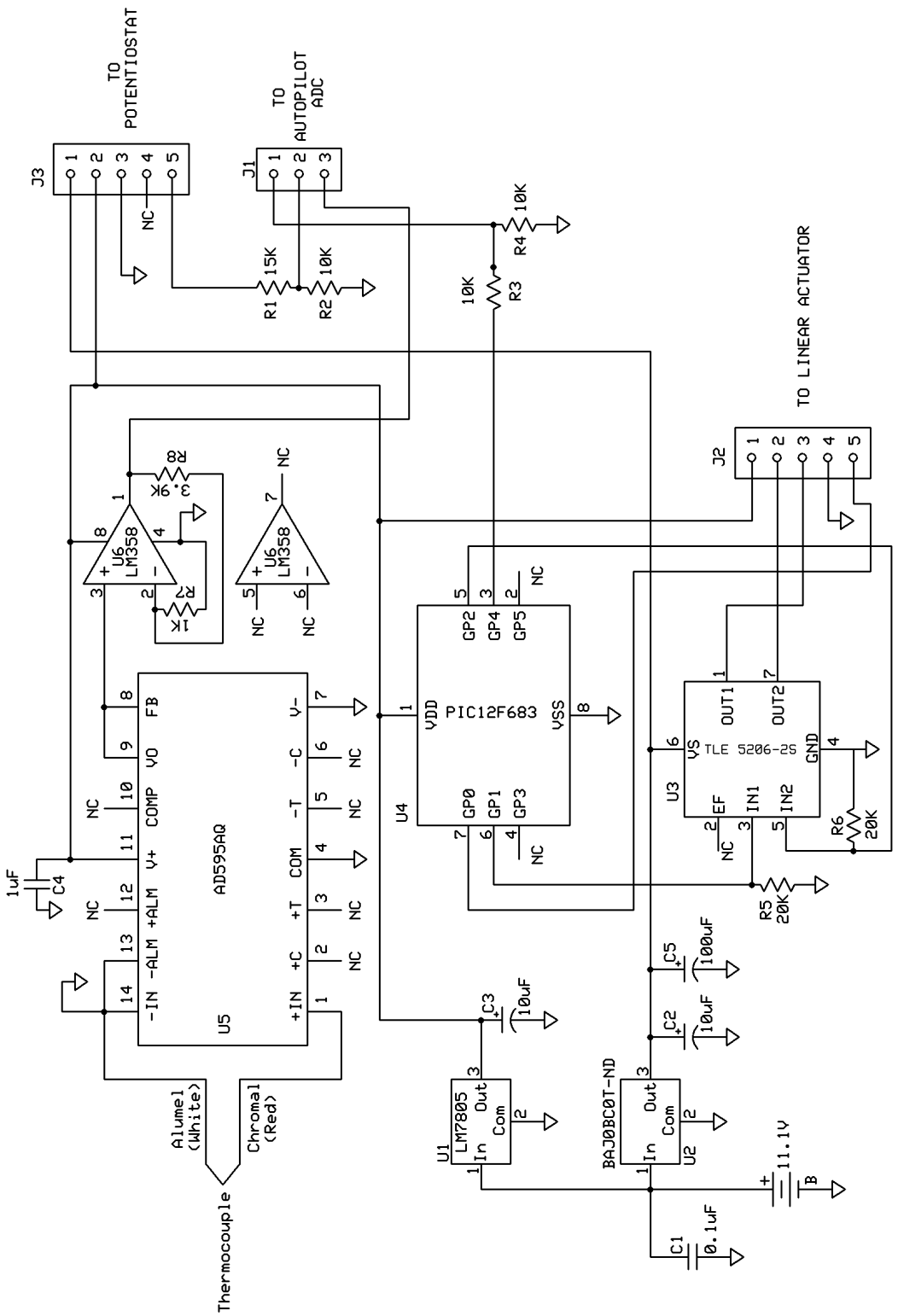

Figure 2.10. Schematic of custom circuit card.

The regulated 5 *volts* was used to power the microprocessor, linear actuator, thermocouple converter, and amplifier. The regulated 10 *volts* was used to power the motor driver. Finally, the CO sensor was powered through this circuit card. The CO sensor circuitry requires ± 5 *volts*. Ten *volts* were supplied to the +5 *volts* pin for the sensor, +5 *volts* to the ground pin, and battery ground to the -5 *volt* pin, effectively creating a ± 5 *volts* voltage supply about a virtual ground for the sensor circuitry.

Although the sensor was supplied ± 5 *volts* about a virtual ground, the sensor output relative to the battery ground was much higher. For a CO concentration range of $0 - 200$ *ppm* the sensor circuitry was calibrated to produce a signal range of $0 - 3$ *volts* with reference to the virtual ground. When compared to the battery ground the voltage range increased to $5 - 8$ *volts*. These voltages were greater than the acceptable measurement range of the ADC port on the autopilot, $0 - 3.2$ *volts*. To overcome this problem a voltage divider was used to reduce the signal to an appropriate range. With the chosen voltage divider the output signal from the sensor was reduced to $2 - 3.2$ *volts*. This was the voltage range that would be detected by the autopilot ADC and corresponded to the original voltage range of $0 - 200$ *ppm*.

A programmable microprocessor was used to control the function of the linear actuator which was used to open and close the valves of the air sample capture device. The linear actuator consists of an extendable arm, a motor, and a potentiometer. The motor both extends and retracts the arm. The potentiometer is attached to the arm and is used to determine the position of the arm. The microprocessor is programmed to instruct the actuator to extend and retract at predetermined intervals. The timer in the microprocessor is a 16-bit timer and it time scale is in milliseconds. Therefore, the maximum length of the programmed timer, and thus time between opening and closing, is approximately 65 *seconds*. At the predetermined time the microprocessor instructs the actuator motor, through the motor driver, to extend or retract the arm until the potentiometer reaches the preset value. The microprocessor monitors the position of the potentiometer to determine when the desired position is reached.

Due to the fact that the CO sensor is sensitive to pressure and temperature changes, it was necessary to monitor these atmospheric conditions for use during

postprocessing. The autopilot already monitors the barometric pressure, but not the air temperature. Thus, it was necessary to include a thermocouple with the custom circuit card. In order to produce a signal that was easily measured, a thermocouple amplifying chip was used. With the expected temperature ranges the thermocouple amplifier output would range from 0 to 0.5 *volts*. An additional noninverting amplifier was used to increase the output so that 0 to 2.45 *volts* corresponds to the same temperature range.

2.3 Aircraft Layout

Finally, the aircraft, autopilot and associated avionics, pollution measurement device, and custom control/interface circuit card were brought together in a final assembly. A three-dimensional computer aided design (CAD) model of the assembly was built in order to ensure that all of the components fit onto the aircraft properly when manufactured. Figure 2.11 shows the complete SAMI aircraft.

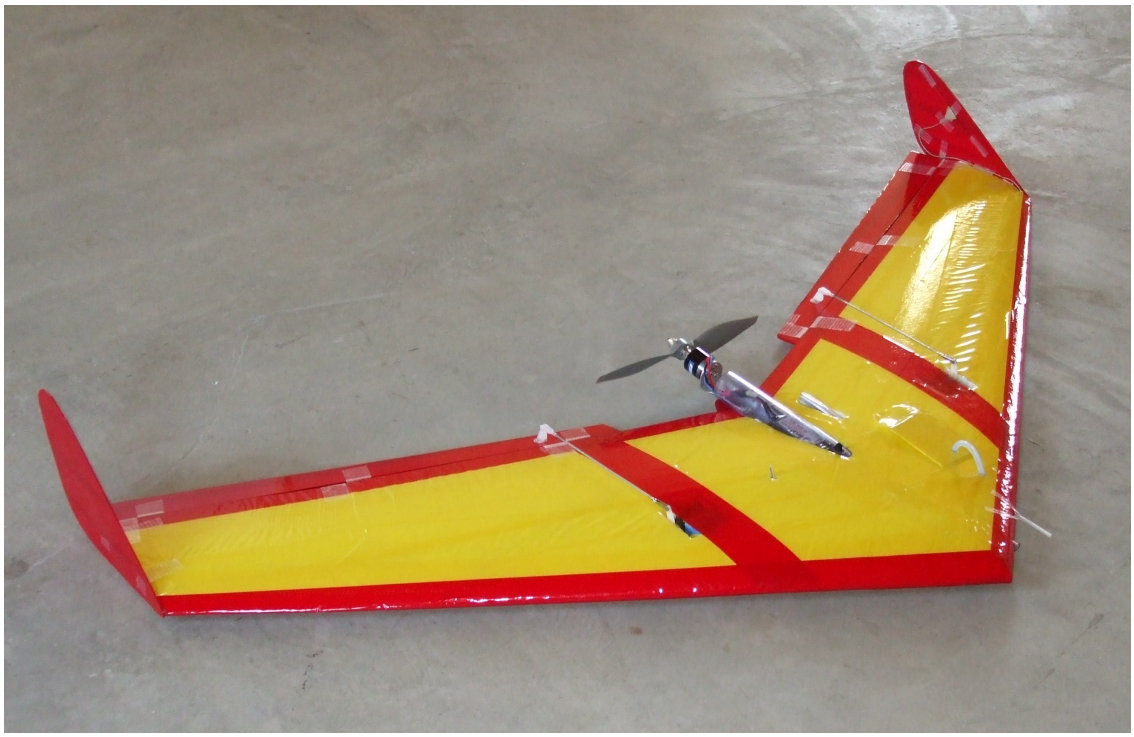

Figure 2.11. Photograph of completed SAMI aircraft.

CHAPTER 3

STATIC PRESSURE ANALYSIS

One of the novel aspects of the present design is to use the existing static pressure difference over the wing surface to drive flow through the chamber. This eliminates the need for a separate pump assembly that must be carried on the aircraft. In order to assess the feasibility of this concept, tests examining the distribution of static pressure along the wing were performed. The results were used to calculate the expected flow rate through the pollution measurement device as well as determine the appropriate gas sampling inlet/outlet locations on the wing surface. Both experimental and computational fluid dynamics (CFD) modeling methods were employed.

3.1 Wind Tunnel Testing

As part of the SAMI design process is was necessary to identify appropriate locations on the wing surface to place inlet and outlet taps for pollution gas sampling. The goal was to find two locations on the aircraft that yielded a high enough pressure difference to maintain flow through the valve near the target flow rate.

3.1.1 Buckingham Pi Analysis

In order to determine the pressure profile of the aircraft a model was tested in the aerodynamic wind tunnel used in the Physical Fluid Dynamics (PFD) Lab at the University of Utah. Due to the size restrictions of the available wind tunnel a full-scale aircraft could not fit. Therefore, a scale model was tested. A Buckingham Pi analysis was performed in order to determine which dimensionless groups would be needed to correlate parameters on the model with those on the full-scale prototype. Appendix B outlines the analysis process used. As a result of the analysis it was determined that

$$Re_m = Re_{fs} \tag{3.1}$$

and

$$C_{p_m} = C_{p_{fs}} \tag{3.2}$$

where Re is the Reynolds number, C_p is the pressure coefficient, the subscript m refers to the scaled model, and the subscript fs refers to the full-scale prototype. Thus, in order to obtain an accurate pressure profile for the full-scale aircraft both the Re and C_p values for the model and full-scale plane much be matched.

The Reynolds number is defined as

$$Re = \frac{\rho \bar{V}_\infty c}{\mu} \tag{3.3}$$

and the pressure coefficient is defined as

$$C_p = \frac{\Delta P}{\frac{1}{2}\rho \bar{V}_\infty^2} \tag{3.4}$$

where $\bar{V}_\infty$ is the average free-stream velocity, ΔP is the local pressure minus the free-stream pressure and c is the chord length along the centerline of the aircraft. Substituting equation (3.3) into equation (3.1) we obtain

$$\frac{\rho_m \bar{V}_{\infty,m} c_m}{\mu_m} = \frac{\rho_{fs} \bar{V}_{\infty,fs} c_{fs}}{\mu_{fs}}. \tag{3.5}$$

Solving equation (3.5) for V_m

$$\bar{V}_{\infty,m} = \bar{V}_{\infty,fs} \frac{c_{fs}}{c_m} \frac{\rho_{fs}}{\rho_m} \frac{\mu_m}{\mu_{fs}}. \tag{3.6}$$

From equation (3.6) we see that the wind tunnel airspeed needed to properly test the model was proportional to the ratio of the chord lengths and was also dependent on the density and viscosity of the air during testing and during actual flight.

The value of ρ can be determined using the ideal gas law (Fox *et al.*, 2004)

$$P = \rho R T \tag{3.7}$$

where P is the barometric pressure of the air, R is the gas constant for air, and T is the absolute temperature of the air. Rearranging equation (3.7) to solve for ρ

$$\rho = \frac{P}{RT}. \tag{3.8}$$

The value of μ can be determined by using the Sutherland equation (Fox *et al.*, 2004)

$$\mu = \frac{b T^{1/2}}{1 + S/T}. \tag{3.9}$$

For air $b = 1.458 \times 10^{-6} \ \frac{kg}{m\,s\,K^{1/2}}$ and $S = 110.4 \ K$. Note, as seen in equations (3.8) and (3.9) that ρ is dependent on air pressure and temperature and μ is dependent solely on temperature.

3.1.2 Test Setup

The test setup consisted of a scaled model of the Unicorn aircraft, mounting sting, pitot-static tube, wind tunnel, pressure transducer, digital scopemeter, stop watch, and thermometer. The aircraft model was rigidly mounted to the sting and the sting rigidly mounted to the ceiling of the wind tunnel as shown in Figure 3.1.

The model used for the wind tunnel testing was printed on an Objet three-dimensional printer located at L-3 Communications - CSW. The printer lays down and cures a very thin layer of plastic-like material on each pass. As each layer is completed, the printing tray drops down the appropriate distance so that the next

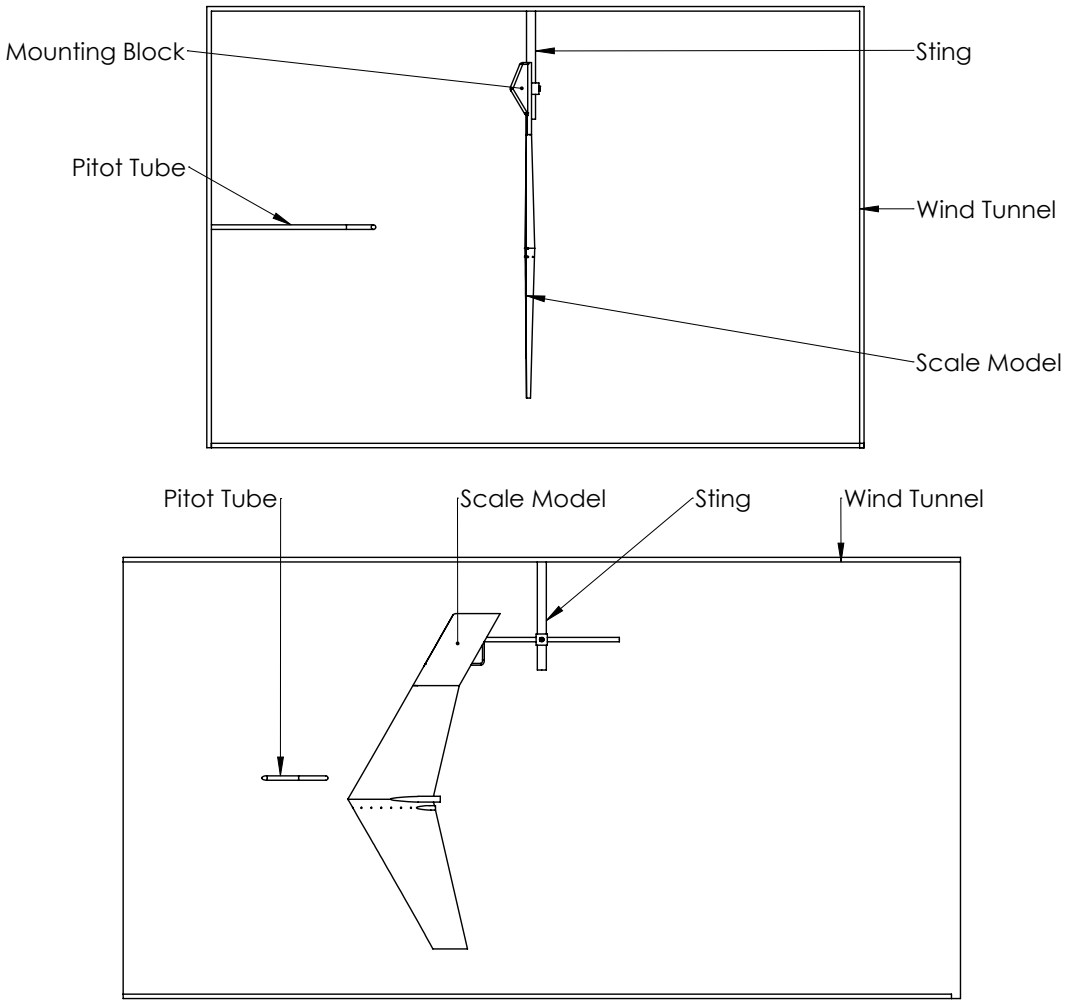

Figure 3.1. Wind tunnel components and setup (front view and side view).

layer can be printed. The printer uses two types of material during printing. The first material is the *model material*. This is the material used to print the actual model structure. Objet printers can print a variety of materials in a variety of colors. The second material is called *support material*, which is a very soft material used to support the model material structure, such as over cavities. Upon completion of the print job, the support material is cleaned off, leaving only the model material. Because of the method used in three-dimensional printing, very complex geometries that would be impossible using traditional manufacturing methods are feasible.

The wind tunnel model consists of a scaled-down (factor of 0.35) version of the Unicorn aircraft with an added mounting block on the right wing tip to facilitate attachment to the wind tunnel support sting. Figure 3.2 shows the corresponding CAD drawing of the wind tunnel model. A set of pressure taps were located along a cross-section of the model that corresponded to the centerline of the pollution measurement device in the full-scale aircraft. The pollution measurement device was located slightly off-center as the center section of the aircraft was occupied by the battery, a circuit card, and an assortment of wires. The centerline of the device

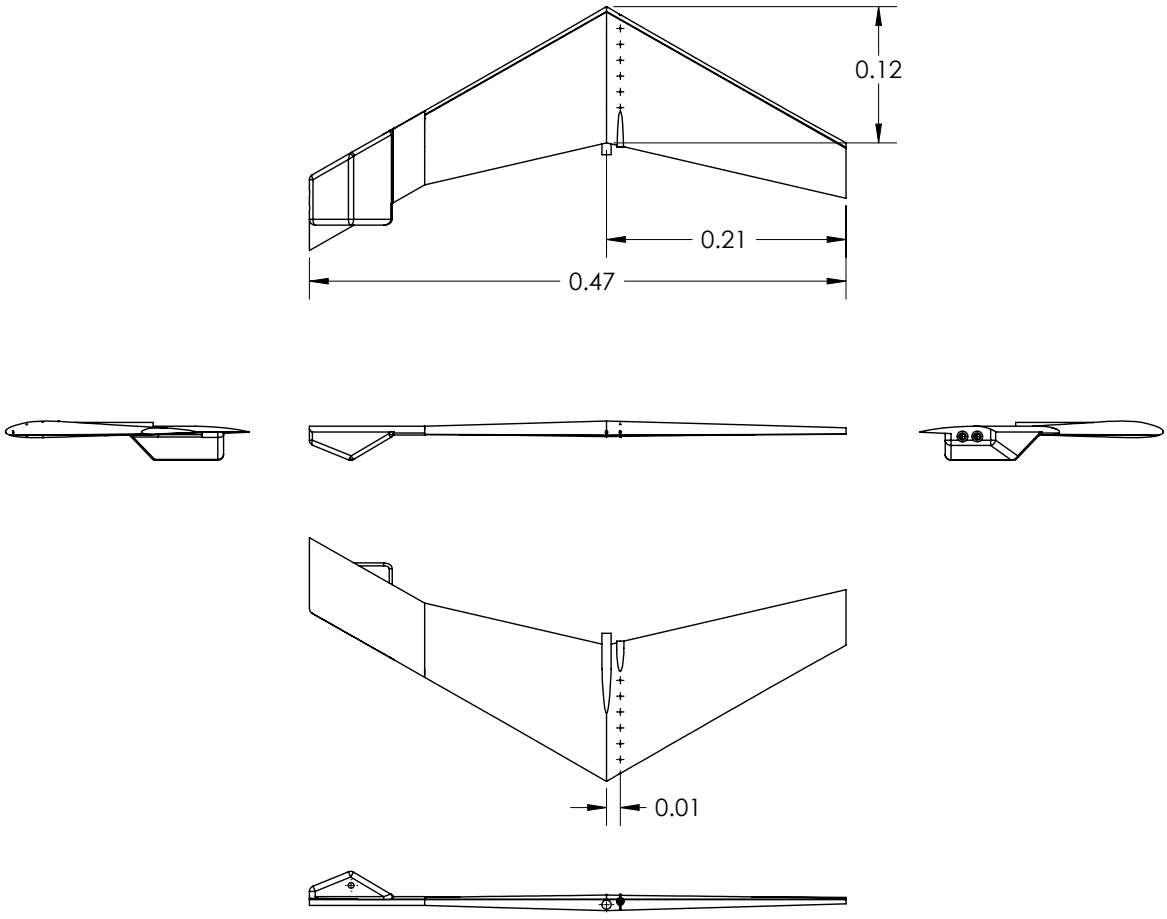

Figure 3.2. CAD drawing of wind tunnel model. Units are in m.

was located approximately 35 mm from the centerline of the aircraft. On the scaled wind tunnel model that corresponded to 12.2 mm from the centerline of the aircraft. The anticipated location of the inlet and outlet taps was along this designated cross-section. A series of 14 pressure taps were inserted into the model. An additional tap was placed into the tip of the nose of the aircraft. The numbering sequence used to identify the pressure taps is shown in Figure 3.3 The corresponding distance of each tap with respect to the leading edge is listed in Table 3.1.

The use of a three-dimensional printer allowed tubes to be designed inside of the wing. The interior tubes ran from the surface pressure taps, along the length of the

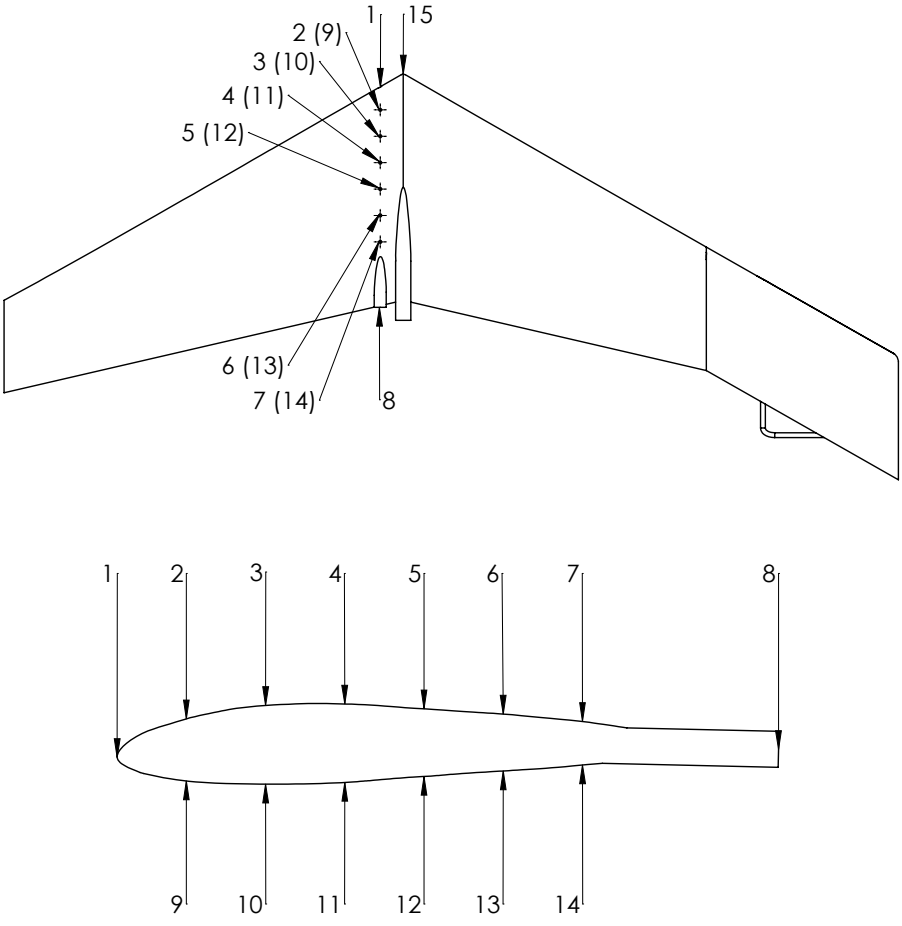

Figure 3.3. Numbering sequence used to label pressure taps on the wing surface.

Table 3.1. Location of each pressure tap with reference to the leading edge.

Pressure Tap	Location (x/c)
1	0
2, 9	0.11
3, 10	0.22
4, 11	0.35
5, 12	0.47
6, 13	0.60
7, 14	0.72
8	1

wing, and through the mounting block. Connectors on the mounting block were used to run external tubes from the wing to the pressure transducer. Note, pressure taps 1 and 15 were routed internally to the same tube, while taps 2-14 were all routed together to a second tube. This is shown in Figure 3.4. During testing, the openings of all but two taps were covered with tape (typically either tap 1 or 15 was left exposed as well as one of the remaining taps).

The chord length of the full-scale Unicorn aircraft, c_{fs}, was measured to be approximately 0.34 m, which translated into a model chord length of 0.12 m (using

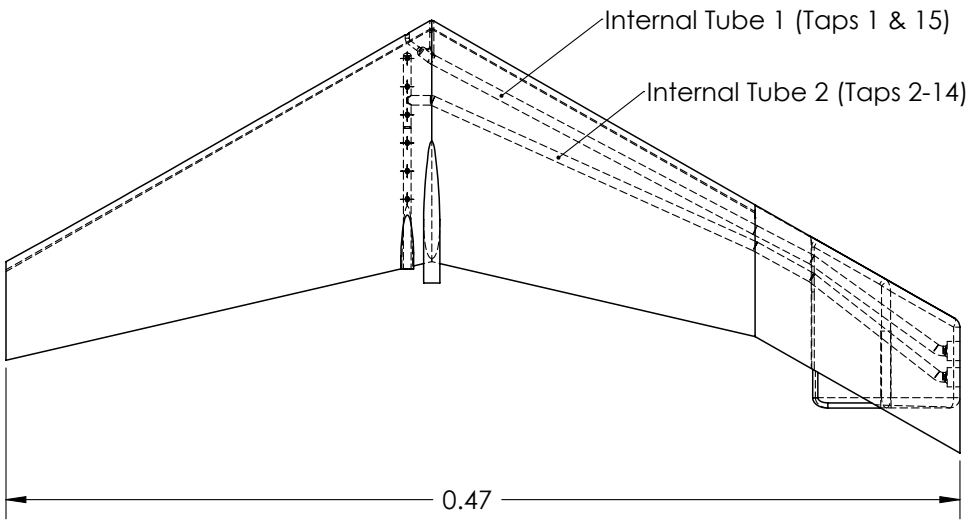

Figure 3.4. View of internal pressure routing tubes. Units are in m.

a 0.35 scale factor). The typical cruising speed of the actual full-scale Unicorn is about 14 m/s, which with local Salt Lake City properties corresponds to an Re value of 2.9×10^5 as calculated using equation (3.3). In order to exactly match the Re number, the required wind tunnel velocity was determined to be 42.3 m/s using equation (3.6) and anticipated air properties in the Fluids Lab.

Unfortunately, this value exceeded the capability of the available wind tunnel, which had a maximum speed of about 30 m/s (corresponding to a speed of 9.6 m/s for the full-scale aircraft). Because the prototype Reynolds number could not be matched in the laboratory, experiments were conducted a three lower Re vlues and the subsequent results were used to validate numerical simulations using the Re of interest. The Re values tested are shown in Table 3.2 along with the corresponding wind tunnel and full-scale airspeeds.

3.1.3 Test Results

Based on Bernoulli's equation the free-stream velocity of the flow was determined using the equation

$$\bar{V_\infty} = \sqrt{\frac{2\left(p_{\infty,0} - p_\infty\right)}{\rho}} \tag{3.10}$$

in conjunction with a pitot-static tube, where $p_{\infty,0}$ is the stagnation pressure and p_∞ is the static pressure, both in the free-stream. A pitot-static tube mounted to the side wall of the wind tunnel was used for this purpose.

Pressure readings were acquired using a *MKS-Baratron Differential Pressure Transducer and Display Unit (Model 398)* which has a range of $0 - 10\ Torr$. The output

Table 3.2. Wind tunnel velocities used during testing along with the corresponding Re and velocity of the full-scale aircraft.

Wind Tunnel (m/s)	Re	Full Scale (m/s)
17.0	1.1×10^5	5.5
23.3	1.6×10^5	7.6
29.9	2.0×10^5	9.6

was connected to a *Fluke 97 Scopemeter*, in which 1 *volt* corresponded to 1 $mm\,Hg$. The scopemeter has the ability to average voltage readings over a prescribed time. In the present experiment each pressure reading was averaged for 30 *seconds*.

In order to minimize the effects of variation in the results due to the mounting of the model two tests were conducted at each of the three Re values listed in Table 3.2. The values of ρ and μ for air corresponding to each data point collected were calculated using equations (3.8) and (3.9), respectively.

The pressure coefficient, C_p, was calculated for each data point using equation (3.4). As two tests were performed at each Reynold's number, the two values of C_p obtained for each pressure tap were averaged. The results are presented in Table 3.3. Figure 3.5 shows a plot of that data provided in Table 3.3, with the exception tap 15.

Of taps 1 through 14 the highest C_p value occurred at tap 1, which is located on the leading edge of the wing. Of the remaining taps, in general the taps on the top surface of the wing had lower C_p values than the taps on the bottom surface. This trend was expected, as an airfoil in a flow creates a lower pressure on the top surface than it creates on the bottom surface of the wing.

As the Reynold's number of the actual full-scale aircraft could not be achieved

Table 3.3. Average C_p values for the wing.

Pressure Tap	$Re = 1.1e5$	$Re = 1.6e5$	$Re = 2.0e5$
1	0.77	0.77	0.77
2	-0.16	-0.16	-0.20
3	-0.40	-0.41	-0.45
4	-0.36	-0.37	-0.41
5	-0.26	-0.27	-0.30
6	-0.22	-0.23	-0.25
7	-0.20	-0.23	-0.25
8	-0.11	-0.11	0.10
9	-0.34	-0.34	-0.30
10	-0.28	-0.27	-0.25
11	-0.24	-0.24	-0.21
12	-0.14	-0.12	-0.09
13	-0.07	-0.05	-0.03
14	-0.02	0.01	0.03

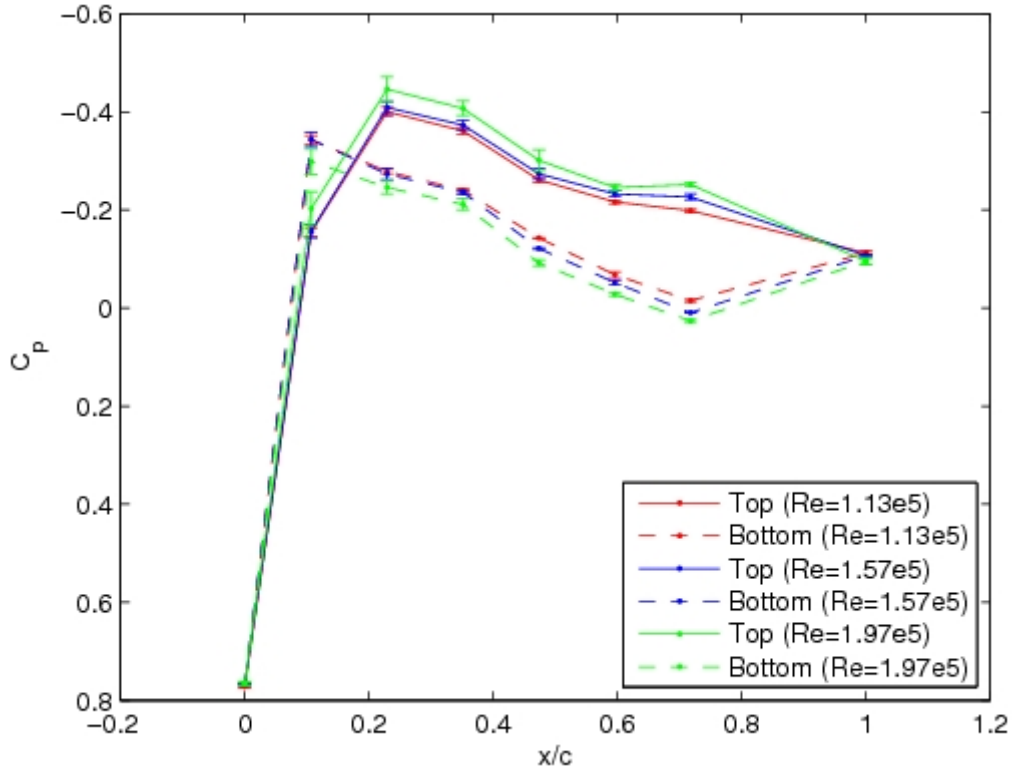

Figure 3.5. Wind tunnel model pressure profile results.

by the wind tunnel, the C_p results were used to optimize the numerical simulations performed in Section 3.2.

3.2 Numerical Simulations

Because of the inability to achieve complete dynamic and geometric similitude in the laboratory experiments,* complementary numerical simulations were performed using Fluent (a commercially available software package for modeling fluid flow with complex geometries). The numerical simulations approximated the static pressure distribution over the wing in steady state conditions.

Three simulations were performed. The first simulation was used to validate the numerical model against the wind tunnel results. In this case, the numerical model

*Recall that the highest model Reynolds number realized in the wind tunnel was still 30% lower than the prototype Reynolds number, and that the wingtip of the wind tunnel model had to be altered to facilitate mounting to the support sting.

utilized the same wing (with additional mounting features) as that employed in the laboratory experiments, and was run at the same Reynolds number as that of the highest run in the laboratory ($Re = 2.0 \times 10^5$). The results of the wind tunnel test and this simulation were compared in order to ensure that the simulation modeled the actual test as accurately as possible. The second simulation used a CAD application of the actual full-scale Unicorn wing and was run at the highest wind tunnel Reynolds number of $Re = 2.0 \times 10^5$. The results from this simulation were compared to the first simulation to identify any possible adverse affects of the mounting block on the pressure profile in the area of concern. The final simulation was of the actual full-scale aircraft again but at the prototype Reynolds number of $Re = 2.9 \times 10^5$.

The three-dimensional CAD model for each case was imported into Gambit to prepare the domain and mesh needed to run the simulations. In order to simulate the flow of air over the aircraft, a rectangular cuboid was created, which was subsequently divided into three subdomains: the Inner Box, the Outer Box, and the Flow Domain. Figures 3.6 and 3.7 illustrate the relative sizes of the subdomains, while Table 3.4 lists the corresponding dimensions and mesh interval spacings. The model aircraft was surrounded by the Inner Box. This subdomain had the finest mesh (highest spacial resolution) of the three subdomains in order to yield accurate calculations of the surface pressure along the wings. Surrounding the Inner Box was the Outer Box. The Outer Box had a slightly coarser mesh compared to the Inner Box. Finally, the Flow Domain surrounded the Outer Box. The Flow Domain had the coarsest mesh of the three subdomains. This scheme of hierarchical interval spacing maintained the highest resolution directly around the aircraft while reducing the overall number of nodes.

Note, the initial mesh interval spacing used for the Inner Box was approximately 1/20 of the principal chord length of the aircraft. The Outer Box was about three times the spacing of the Inner Box and the Flow Domain was three times the spacing of the Outer Box.

The turbulence was modeled using the Spalart-Allmaras model. The Spalart-Allmaras turbulence model was initially designed for use with aerospace applications

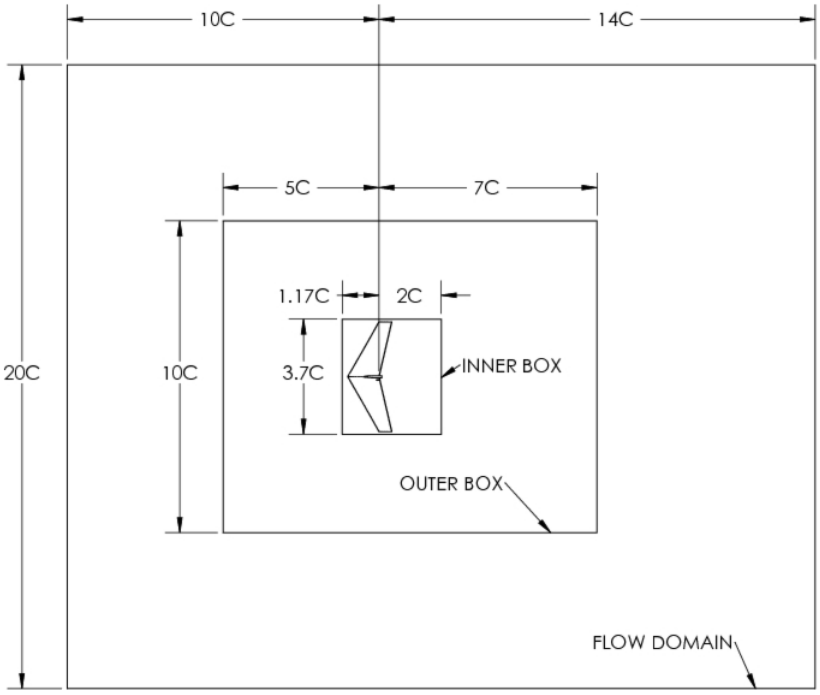

Figure 3.6. Top view of airflow domain used for CFD analysis. All dimensions are expressed proportional to the principle chord length of the aircraft, *c*.

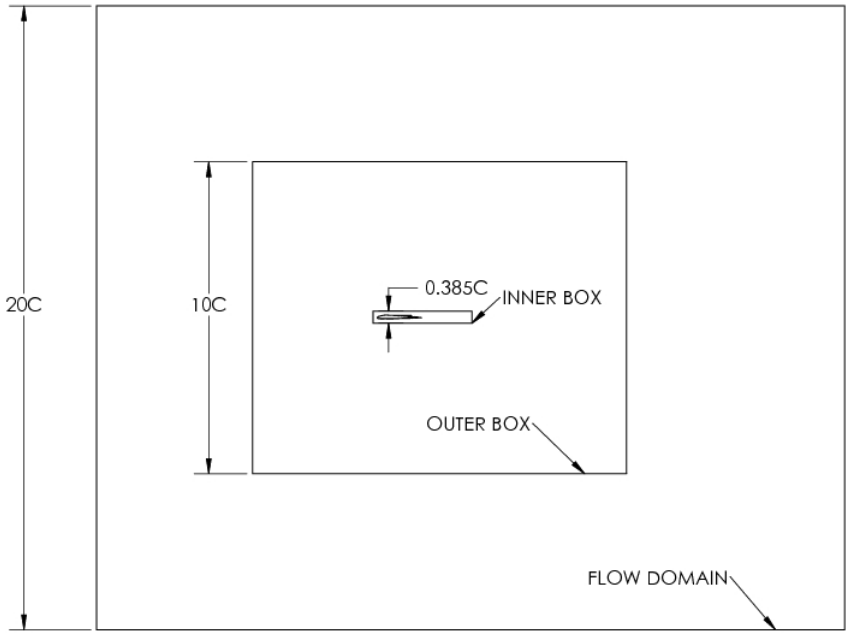

Figure 3.7. Side view of airflow domain used for CFD analysis. All dimensions are expressed proportional to the principle chord length of the aircraft, *c*.

Table 3.4. Airflow domain sizes.

Domain	Length (mm)	Width (mm)	Height (mm)	Initial Mesh Interval (mm)
Inner box	1089	132	1267	15
Outer box	4116	3430	3430	50
Flow domain	8232	6860	6860	150

and results published in the original work showed acceptable application of the model to airfoils (Spalart & Allmaras, 1992). Also, as the Spalart-Allmaras model is a one-equation model, less time was required to execute the numerical simulation (Wilcox, 2006). Wilcox also states that "Spalart-Allmaras predictions are satisfactory for many engineering applications" and are "especially attractive for airfoil and wing applications, for which it has been calibrated" (2006).

Air properties were assumed to have constant values of 1.06 kg/m^3 for density and $1.77e^{-5}$ $kg/m \cdot s$ for viscosity. For the first two simulations the operating pressure was set to 86448 Pa which corresponded to the expected pressure at an altitude of 1320 m, the average altitude in Salt Lake City where the lab is located. For the third simulation the operating pressure was set to 85400 Pa which corresponded to the expected pressure at an altitude of 1420 m, typical of 100 m above ground level in Salt Lake City. The boundary conditions used are shown in Figure 3.8. The surfaces of the SAMI aircraft were defined as a wall. The Flow Domain face directly in front of the aircraft and the four faces surrounding the sides were defined as velocity inlets with a single velocity in the X-direction being defined. Lastly, the Flow Domain face behind the aircraft was defined as a pressure outlet.

Each model was run at one of two different inlet velocities. The first two simulations were run at $\bar{V}_\infty = 9.6\, m/s$, which corresponded to the highest Reynolds number attainable by the wind tunnel, $Re = 2.0 \times 10^5$. The third simulation was run at 14 m/s (typical of the average cruising speed of the actual aircraft), which corresponded to the Reynolds number of $Re = 2.9 \times 10^5$.

During the analysis the mesh was refined twice. The first refinement was performed manually by reducing the aircraft surface mesh interval spacing from 15 mm

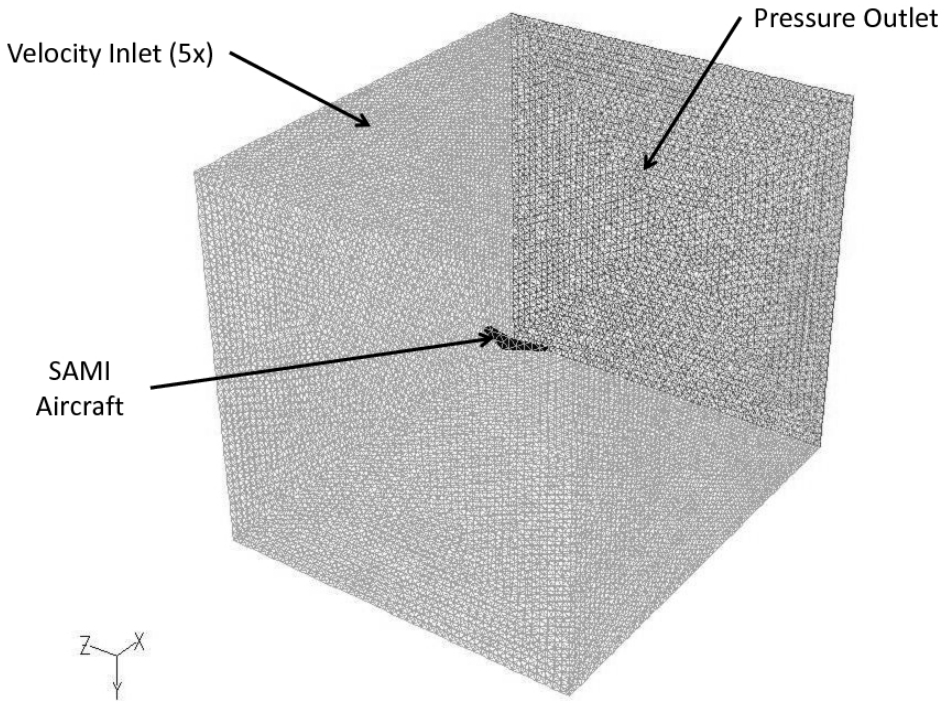

Figure 3.8. Numerical simulation boundary conditions.

to 5 mm. The second refinement was achieved using the adapt function in Fluent, whereby the mesh interval spacing in the affected areas was further reduced to 2 mm. Figure 3.9 shows the original mesh surrounding the aircraft, and Figure 3.10 shows the mesh after the second refinement. The following results were obtained using the finest mesh.

3.2.1 Results

Static pressure and velocity data from the simulations were used to calculate the local pressure coefficient, C_p, from equation (3.4) at the same locations on the wing as the pressure taps in the wind tunnel experiments. Figure 3.11 shows the results from the from the wind tunnel tests and the first simulation, which was used to verify the accuracy of the numerical simulations as compared to the actual wind tunnel results. The greatest difference in C_p values occurred along the leading edge, where there was a 61% difference. This difference was attributed to the curvature of the model along the leading edge, which proved difficult to mesh well in the simulation.

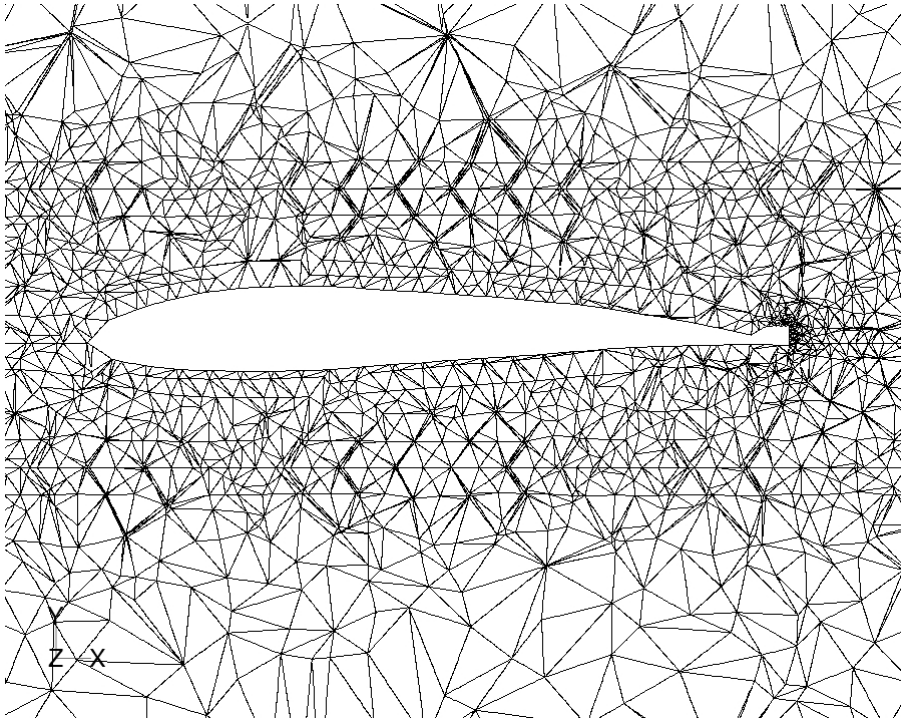

Figure 3.9. Original mesh.

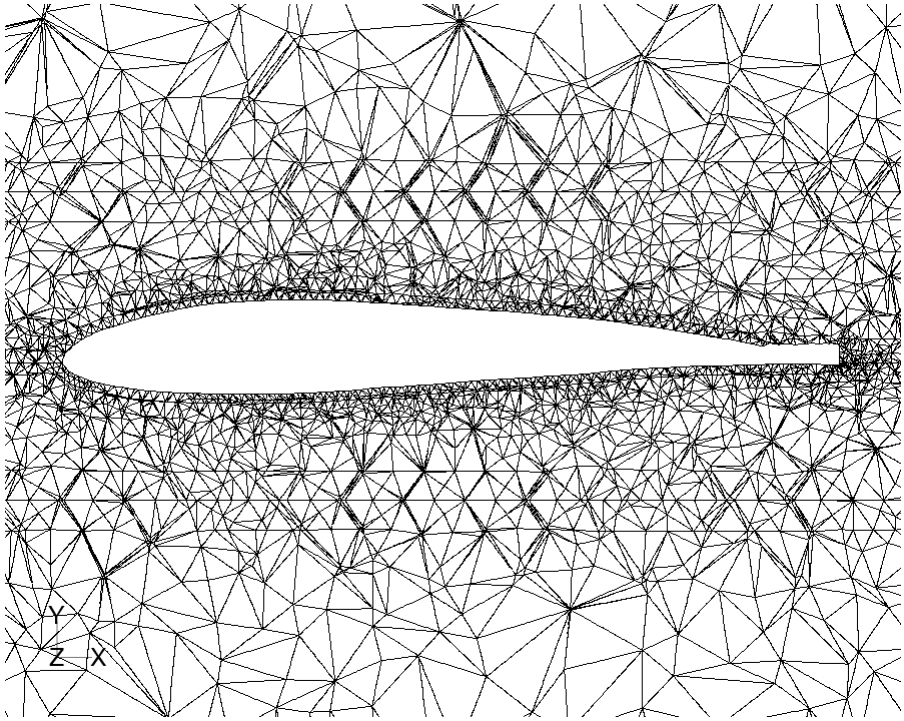

Figure 3.10. Refined mesh.

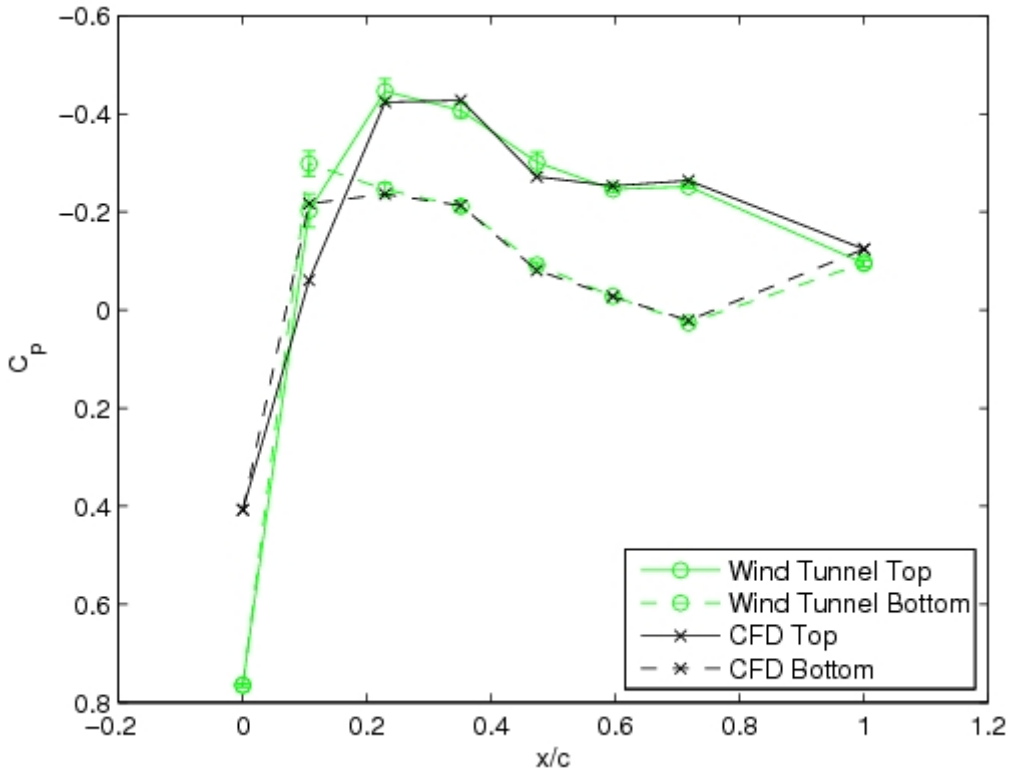

Figure 3.11. Comparison of wind tunnel C_p values with CFD (with wind tunnel geometry) C_p values when $Re = 2.0e5$.

Figure 3.12 compares the results of the first two simulations where both models (i.e., the one having geometry identical to the wind tunnel model, with the added mounting feature along the wing tip, and the other having geometry identical to the actual Unicorn wing) were run at the same Reynolds number, $Re = 2.0e5$. The results in Figure 3.12 reveal negligible variation in C_p values between the two models, except for the rear most tap. At that tap there was a 169% difference in C_p values between the two different model geometries. However, note that this percentage difference is especially large because one of the C_p values is almost 0. Therefore, it may be concluded that the added material along the right wing tip had an insignificant effect on the static pressure near the centerline of the aircraft.

Figure 3.13 shows the results from the third simulation compared to the second simulation. The results from the third simulation are for the actual full-scale model at a Reynolds number of $Re = 2.9 \times 10^5$, which corresponds to the typical cruising

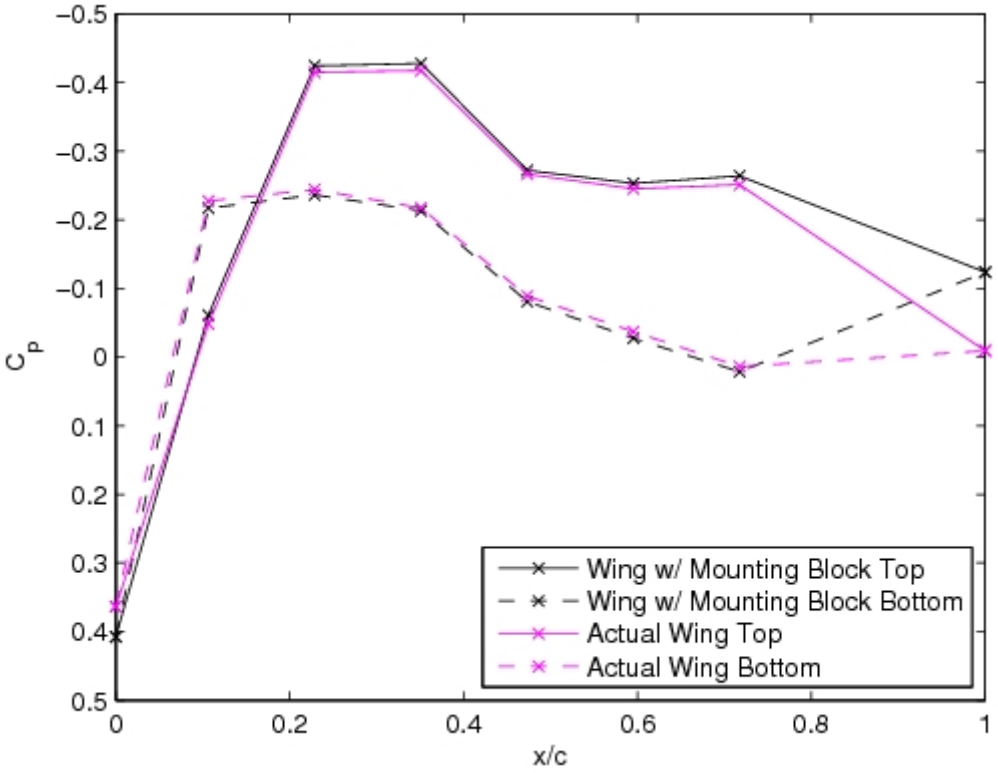

Figure 3.12. Pressure coefficient along the wing surface based on the numerical simulations for the two different model geometries when $Re = 2.0e5$.

speed of 14 m/s for the aircraft. These results represent the expected C_p values for the actual aircraft during actual flight. Figure 3.13 shows that the difference between the results for that actual aircraft when $Re = 2.0 \times 10^5$ and when $Re = 2.9 \times 10^5$ were negligible. The third simulation results were also compared to the original wind tunnel results in Figure 3.14. Figure 3.14 shows that the results of the final simulation closely matched the wind tunnel results.

The results of both the third simulation and the actual wind tunnel test were considered when determining acceptable inlet and outlet locations for the pollution measurement device. Due to the size of the pollution measurement device it was determined that the outlet would be located at a position on the wing where x/c was between 0.5 and 1. Tables 3.5 and 3.6 show the possible inlet/outlet combinations and their corresponding pressure differences based on the third simulation and wind tunnel results respectively. During construction of the SAMI aircraft it became apparent

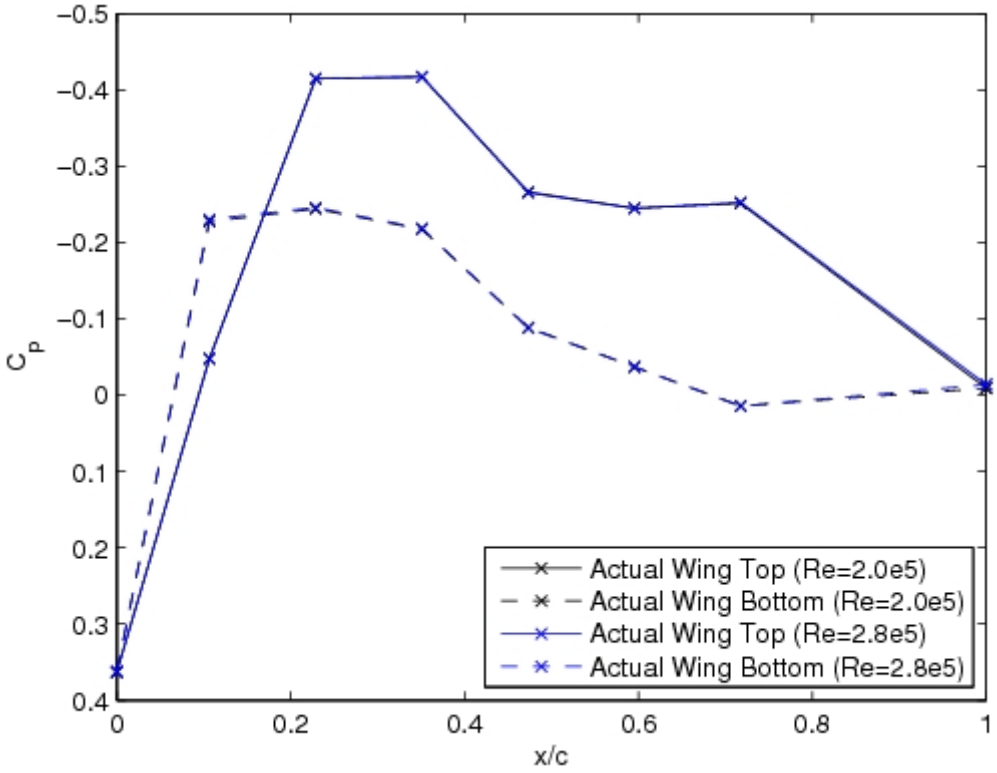

Figure 3.13. Results from CFD simulations for full-scale aircraft.

that a convenient location for the pollution measurement device outlet corresponded to pressure tap 7.

As shown in Table 3.5 the expected pressure difference between taps 1 and 7 is approximately 64 Pa, which corresponds to an average air velocity through the device of 5.5 m/s and a flow rate of 10.5 L/min. From Table 3.6 the expected pressure difference between taps 1 and 7 is approximately 106 Pa. This pressure difference corresponds to an average air velocity through the device of 8.6 m/s and a flow rate of 16.3 L/min. Both the wind tunnel test and numerical simulation results show that a sufficient pressure difference should exist between taps 1 and 7 to drive air through the pollution measurement device.

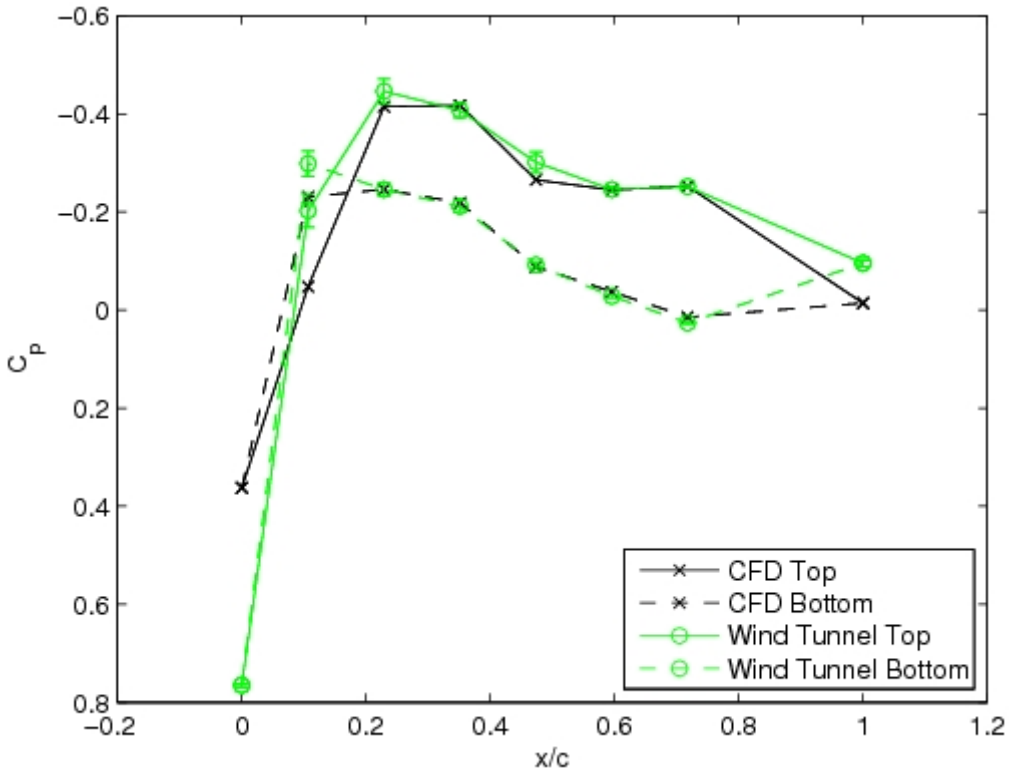

Figure 3.14. Results from CFD simulation for full-scale aircraft ($Re = 2.0e5$) compared to the wind tunnel results ($Re = 2.9e5$).

Table 3.5. Pressure difference between possible inlet/outlet locations with corresponding flow velocity and volumetric flow rate for the actual aircraft based on the final CFD model ($Re = 2.9 \times 10^5$).

Pressure Taps (Inlet→Outlet)	ΔP (Pa)	Velocity (m/s)	Volumetric Flow Rate (L/m)
$1 \rightarrow 5$	65	5.6	10.6
$1 \rightarrow 6$	63	5.5	10.4
$1 \rightarrow 7$	64	5.5	10.5
$1 \rightarrow 8$	39	4.2	8.0

Table 3.6. Pressure difference between possible inlet/outlet locations with corresponding flow velocity and volumetric flow rate for the actual aircraft based on the wind tunnel results ($Re = 2.9 \times 10^5$).

Pressure Taps (Inlet→Outlet)	ΔP (Pa)	Velocity (m/s)	Volumetric Flow Rate (L/m)
$1 \rightarrow 5$	111	8.8	16.8
$1 \rightarrow 6$	105	8.6	16.3
$1 \rightarrow 7$	106	8.6	16.3
$1 \rightarrow 8$	89	7.8	14.8

CHAPTER 4

BENCH-TOP AND FLIGHT TESTING

4.1 Bench-top Testing

Bench testing of the pollution measurement device was performed in order to verify the functionality of the device as well as to characterize its response. The bench test setup included a laptop, 18-channel DAQ, zero-air gas source (0 ppm CO), 200 ppm CO gas source, adjustable mixing chamber, power supply, blower, flow rate controller, and an assortment of tube lengths and wires. The test setup is shown in Figure 4.1. The zero-air and CO gas tanks were connected through pressure regulators and tubes to the adjustable mixing chamber. A flow rate meter and needle valve connected to each inlet allowed a large range of CO concentrations to be mixed efficiently and delivered to the pollution measurement device. The device outlet was connected to a separate flow rate controller, which was also connected to the blower.

By knowing the concentration of the source tanks along with the volumetric flow rate of each of the inlet lines, the resulting outlet concentration could be determined according to

$$C = \left(\frac{Q_g}{Q_{za} + Q_g} \right) C_g \tag{4.1}$$

where C is the outlet concentration, Q_g is the source gas volumetric flow rate, Q_{za} is the zero-air volumetric flow rate, and C_g is the source gas concentration.

4.1.1 Supplying the Required Pressure Drop

In order to accurately mimic the expected operating conditions on the actual full-scale aircraft it was necessary to generate a pressure drop of approximately 100 Pa across the pollution measurement device in the bench-top test setup. This

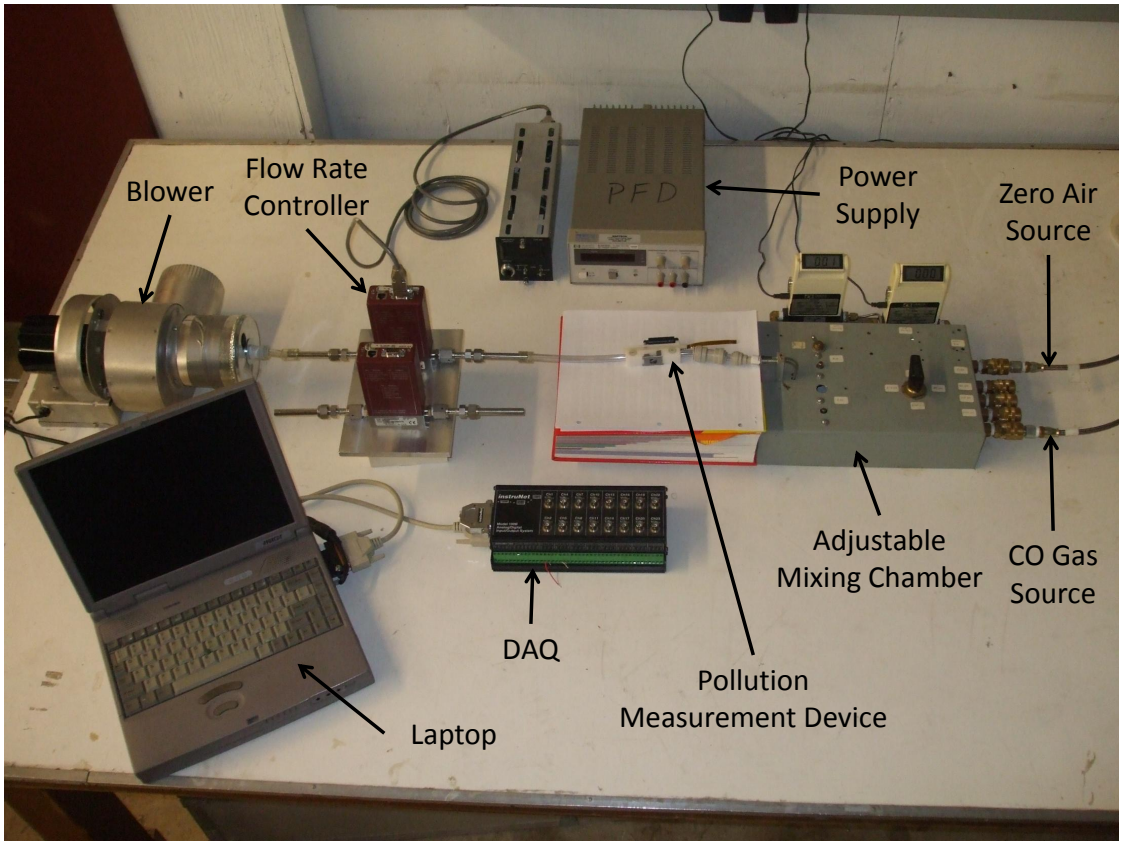

Figure 4.1. Bench-top test setup.

was achieved using configuration shown in Figure 4.1. The blower, in its current state, was able to produce a pressure difference of almost 250 Pa as measured using a manometer. Although the actual pressure difference of the test setup was two and a half times greater than that expected during flight, the pressure difference was within the sealable range of the valves on the pollution measurement device (explained in Section 4.1.3). This pressure difference was only the case when the valves were closed, however.

An air flow rate lower than that expected during flight was used during bench testing as the mixing chamber could not supply a similar air flow rate. However, the pressure of the supplied gas was much greater than the valves could handle. Therefore, a setup similar to Figure 4.2 was used in the line between the mixing chamber outlet and the pollution measurement device inlet. This connection consisted of a connector which had an inner diameter 4.75 mm larger than the pollution measurement device

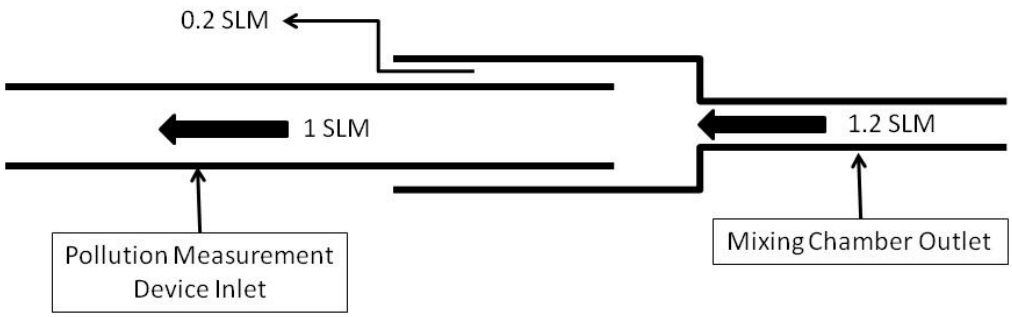

Figure 4.2. Gas overflow connection diagram.

inlet tube. The connector was securely attached to the chamber outlet and the measurement device inlet tube was inserted approximately 75% of the way into the connector. The chamber flow rate was maintained at 1.2 SLM and the flow rate controller restricted the flow rate through the pollution measurement device to 1 SLM. Thus, the 20% excess gas supplied by the chamber flowed around the device inlet and out into the surrounding air, effectively eliminating the pressure applied to the valve. With the use of this connection only the blower forced air to flow through the device.

4.1.2 Preliminary Testing

Preliminary testing of the complete pollution measurement device was performed to evaluate the functionality of the system as designed. The device was programmed to open and close the valves at one minute intervals while the concentration in the supply line was varied in 50 *ppm* increments from 0 to 200 *ppm*. During the procedure, the concentration was adjusted synchronously with the valve opening. The output from the sensor was recorded continuously. Figure 4.3 shows the results from this test.

Each time the valves were opened and the concentration increased it was observed that the sensor output was similar to an exponential-like trend, increasing toward the applied concentration, albeit with a relatively long time constant. However, the output never fully reached the applied concentration during the 60 *seconds* the valves were open. When the valves were closed the sensor output decreased dramatically,

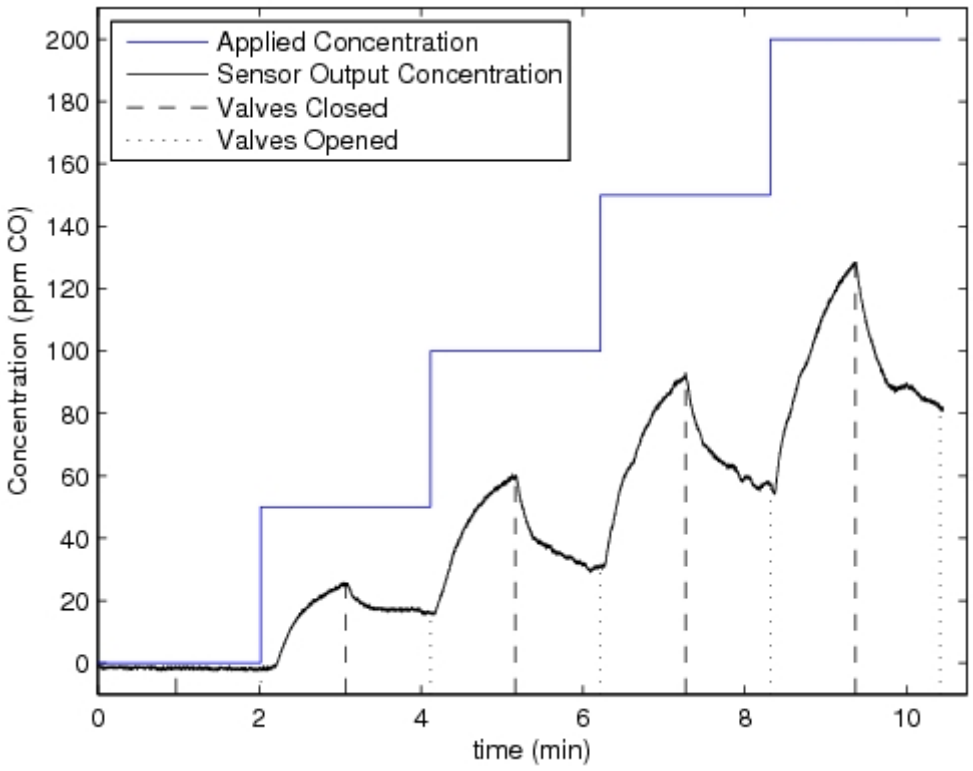

Figure 4.3. Preliminary test results with the original valves: opened (− − −) and closed (· · ·).

contrary to the expected behavior. It was anticipated that when the valves were closed the output would either remain constant or continue increasing toward the supply concentration. Two possible reasons for the observed trend were identified: possible leakage around the valves and/or CO consumption by the sensor. Each of these is discussed in the following subsections.

4.1.3 Valve Design

Upon further examination of the valves, it was observed that the linear actuator did not repeatedly extend/retract to the programmed position. Thus, the valves were not consistently in the same position when opened and closed. With the original valve design, the maximum angular tolerance was calculated to be ±6.4°. This meant that, if the final position of the valves was off by more than 6.4° in either direction, the valves would not be fully closed.

In order to ensure that the valves sealed the device properly, two alterations were made. First, the inner diameter of the valve was decreased from 6.4 mm (1/4 $inches$) to 4.8 mm (3/16 $inches$). This change increased the maximum angular tolerance to $\pm 18.2°$. Second, a rubber-like gasket was designed onto the surface of the valve. The valves were printed on the same Objet 3D printer used to create the wind tunnel model. The printer has the ability to print two different materials during the same job. This capability allowed a 0.6 mm-thick layer of a soft, rubber-like Shore A photopolymer to be added directly to the outer surface of the valve (Obj, 2010). This gasket increased the sealing capability of the valve. Figure 4.4 shows the original valve compared to the redesigned version.

In order to determine if the redesigned valves would sufficiently seal the device a leak test was performed. The setup used to perform the leak test is shown in Figure 4.5. The pollution measurement device, with only the valves installed, was connected to a barbed T-connector. A manometer was connected to one of the other connector ports and pressurized air was applied to the third connector port. The pressure was gradually increased until the valve began to leak, and then subsequently reduced until leaking stopped.

Both the redesigned inlet and outlet valves were tested. The inlet valve reached a

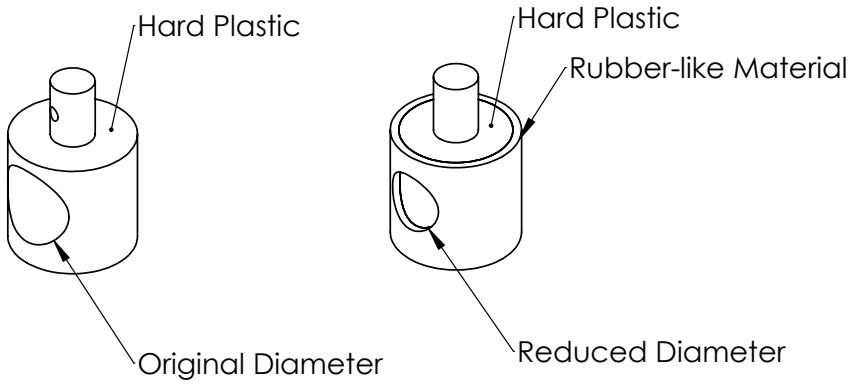

Figure 4.4. Original valve (left) and redesigned valve (right) drawn to scale.

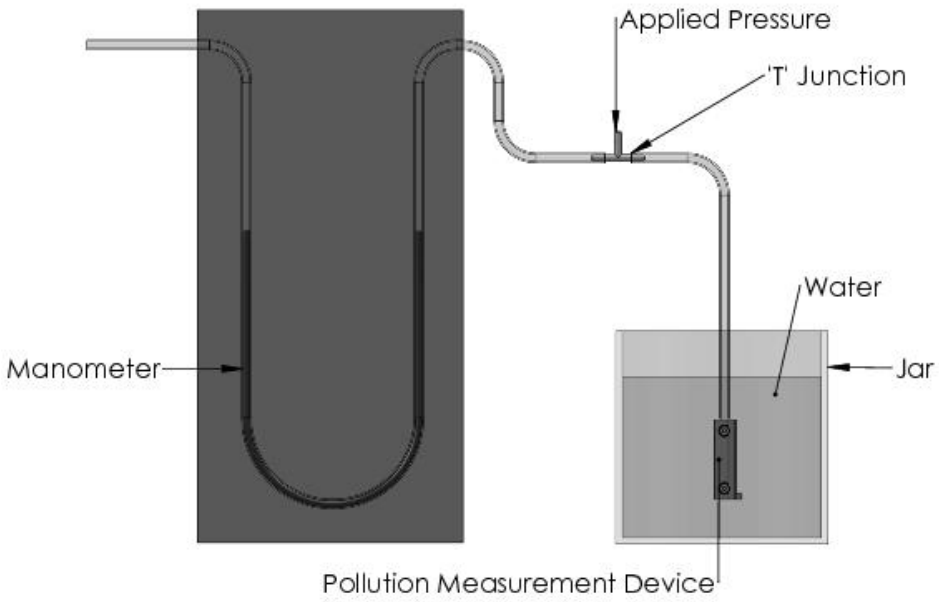

Figure 4.5. Leak test setup.

pressure of 2700 Pa (11 $inches\ H_2O$) before leaking, while the outlet valve reached 1700 Pa (7 $inches\ H_2O$). Thus, the maximum pressure the device could withstand was determined to be 1700 Pa. As stated in Section 4.1.2, the expected pressure to be applied to the valve during flight is 100 Pa. Therefore, the redesigned valves are capable of withstanding pressures up to 17 times greater than those expected during typical flight. The preliminary test, described in Section 4.1.2, was performed again using the redesigned valves. The results of this test are shown in Figure 4.6. The behavior is nearly identical to that observed in Figure 4.3 using the original valves. Therefore, the decay in concentration that occurs upon valve closure cannot be attributed to leakage.

4.1.4 Sensor Consumption

The other possible cause for the unexpected decrease in sensor output during valve closure is consumption of CO gas by the sensor. As described in Section 2.2.3.1 the sensor is an amperometric sensor which produces a current as the target gas is consumed. The current produced is based on the concentration of the gas exposed to the sensing element. Modeling this consumption as a first order, linear system yields

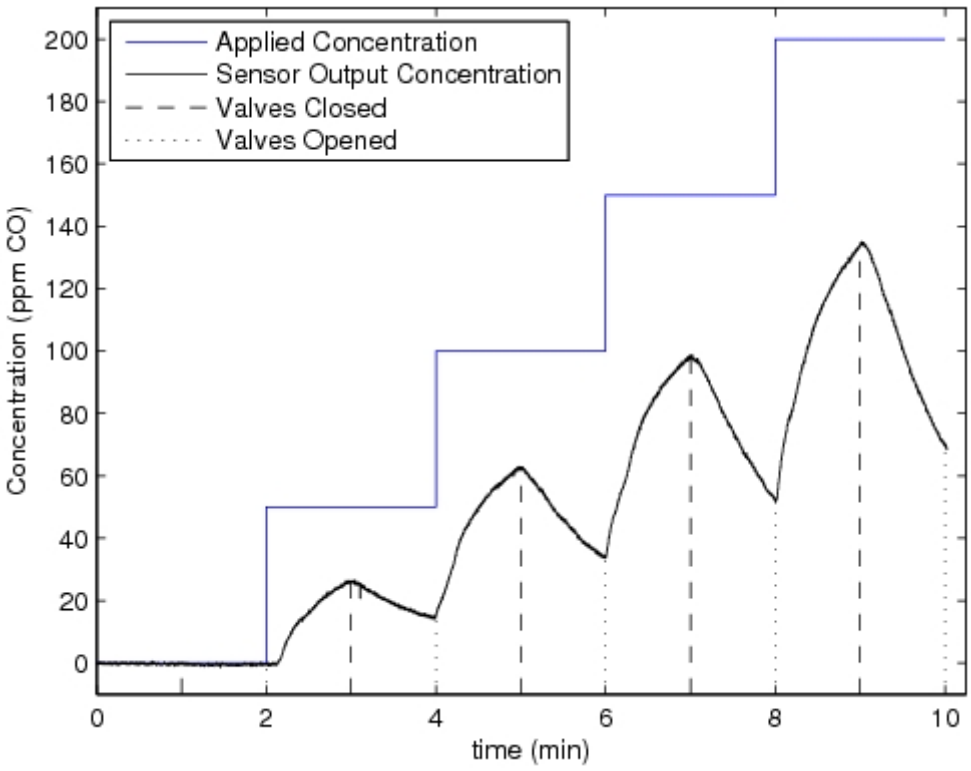

Figure 4.6. Test results using redesigned valves: opened $(- - -)$ and closed $(\cdots)$.

the following prediction for the measured concentration, C, as a function of time, t, during consumption,

$$C = C_0\, e^{-r\, t} \tag{4.2}$$

where C_0 is the initial concentration and r denotes the consumption rate. The parameter r may be determined two ways: (i) experimentally, by fitting the data to equation (4.2) using a least squares method, and (ii) analytically, using the manufacturers specification. The latter was calculated as $r = 5.3 \times 10^{-3} - 8.2 \times 10^{-3}\ 1/s$. Figure 4.7 shows experimental data along with a curve fit superposed. The data were obtained by saturating the sensor with a CO concentration of 200 *ppm* until the output reached steady state, whereby the valves were closed ($t = 60$ *sec* in Figure 4.7). The data between $60 - 120$ *sec* were fit to equation (4.2).

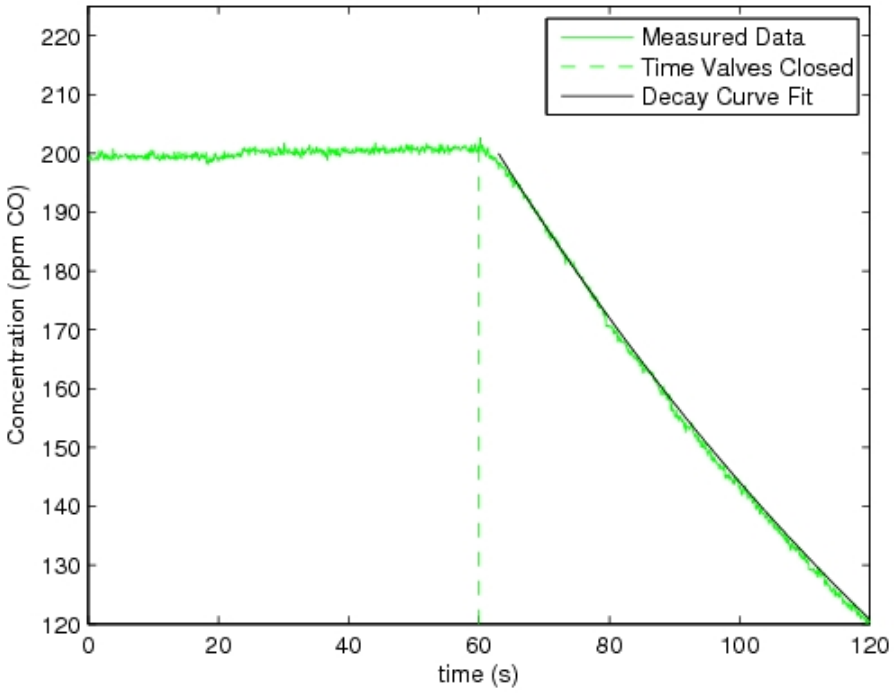

Figure 4.7. Decay test results. Dashed line (−−) indicates when valves were closed.

The corresponding experimental consumption rate was determined to be 9×10^3 $1/s$, which is about 8.9% faster than that predicted using the manufacturer's specification. However, this difference is small enough to reasonably conclude that the observed decay during valve closure is predominately due to CO consumption by the sensor. For example, given a supply concentration of 100 *ppm*, the output would be expected to decrease to 58 *ppm* over a period of one minute while the valves are closed. This agrees well with the observations in the preliminary tests shown in Figure 4.6.

4.1.5 Device Response Time

Another important characteristic of the pollution measurement device is the response time. The response time is defined as the time required for the CO sensor output to reach 90% of the actual value for a constant concentration of the supply gas. The experiment used to determine the response time consisted of applying a step input of known concentration K to the device, and subsequently measuring the

output. The step input was generated by manually raising the supply concentration from 0 *ppm* to a higher concentration, K, as close to instantaneously as possible, via a needle valve, then continuing to maintain that concentration for an extended period of time. Typically 30 *minutes* was necessary before the output plateaued to the value K.

Figure 4.8 presents the resultant response of the device to a step input of CO for three supply concentrations: $K = 40,\ 100$, and 200 *ppm*. Table 4.1 lists the response time for each of the three different step inputs. The maximum response time was approximately 7 *min*. Note, the excessively long response time is due to the presence of an additional filter that minimizes the effects of "misreadings" due to other airborne contaminates, as discussed in Section 2.2.3.1. However, the long response time poses a significant challenge in terms of making real-time measurements during flight. Additionally, there was a great deal of variability in the response time

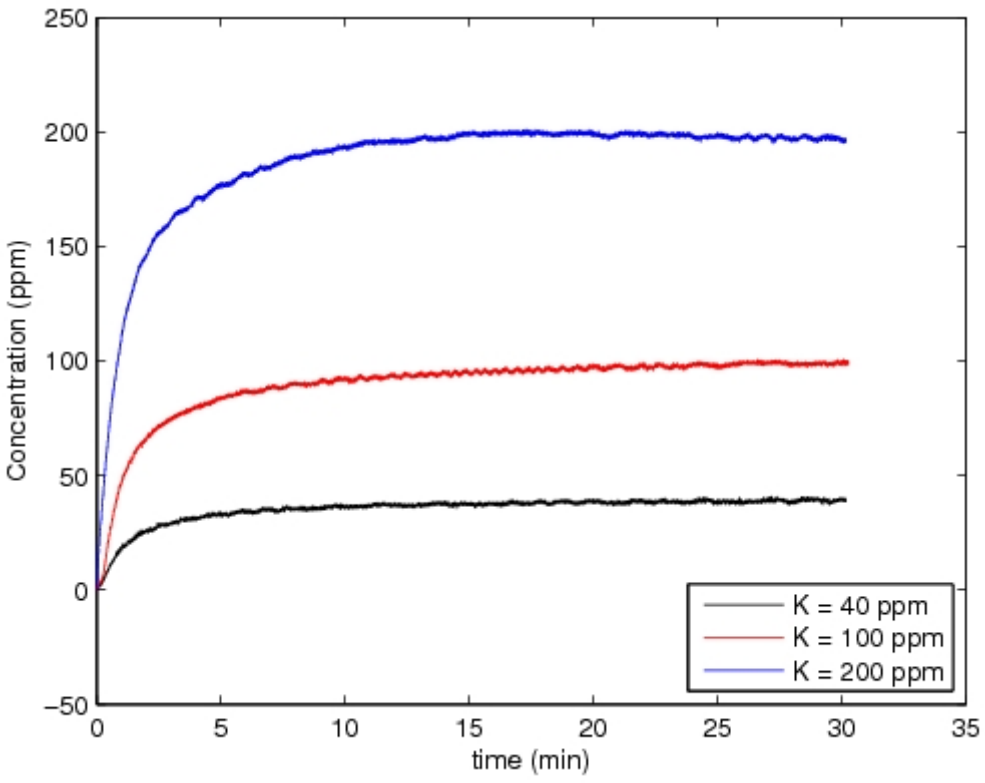

Figure 4.8. System response to a step input in concentration, where K represents the supply concentration.

Table 4.1. Response time of system for three different step inputs.

Applied Concentration (ppm)	Response Time (min)
40	7
100	3-7
200	5-10

from the test. Additional step input tests of 100 ppm had response times as low as 3 $minutes$ and additional step input tests of 200 ppm had response times as long as 10 $minutes$. Future work should include a determination of the factors that affect the sensor output response time. The transfer function for the device was examined as a potential means to overcome the limitations of the long response time.

4.1.6 System Transfer Function

An attempt was made to model the pollution measurement device as a linear system and obtain its corresponding transfer function. The concepts and equations related to transfer functions and Laplace transforms used in this section were obtained from Franklin *et al.* (2002). The basic block diagram is shown in Figure 4.9, both in the time and Laplace domains. Here, $x(t)$ represents the time varying concentration supplied to the sensor, $y(t)$ represents the measured output from the device, $X(s)$ and $Y(s)$ denote the Laplace transform of $x(t)$ and $y(t)$ respectively, i.e. $\mathcal{L}[x(t)] = X(s)$ and $\mathcal{L}[y(t)] = Y(s)$, and $G(s)$ denotes the system transfer function. The idea behind this approach is that, if $G(s)$ could be measured experimentally for a simple step input, then the output could be predicted for any arbitrary input according to

$$X(s)\, G(s) = Y(s)\,. \tag{4.3}$$

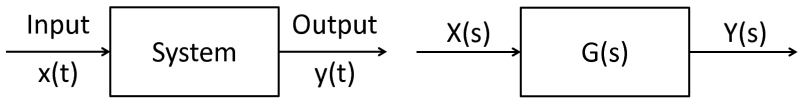

Figure 4.9. Typical system block diagram of a linear system: in the time domain (left) and Laplace domain (right).

In the present application, however, the output is known (measured) while the input remains to be determined. In this context, the time-resolved supply concentration may be calculated by taking the inverse Laplace transform of $Y(s)\ H(s)$ using

$$x(t) = \int_0^t y(t)\, h(t-\tau)\ d\tau, \tag{4.4}$$

where $H(s) = G^{-1}(s)$ and $h(t) = \mathcal{L}^{-1}[H(s)]$. Note, $h(t)$ represents a linear filter that appropriately adjusts the output to account for the inherent time lag in the sensor.

The remainder of the section describes the results from an experiment performed to evaluate the viability of using equation (4.4) to model the pollution measurement device and recover an accurate, time-resolved record of the supply concentration signal. The same data used in Section 4.1.5 were used to determine $G(s)$. Figure 4.8 displays the output for three such tests for $K = 40,\ 100$, and $200\ ppm$. The Laplace transforms of the input, $x(t)$, and output, $y(t)$, were then calculated. For the case of the former, the Laplace transform of a step function is given analytically as

$$\mathcal{L}[x(t)] = X(s) = \frac{K}{s}. \tag{4.5}$$

The Laplace transform of the output was calculated by numerically integrating the following using the trapezoidal rule

$$\mathcal{L}[y(t)] = Y(s) = \int_0^\infty y(t)\, e^{-st}\, dt. \tag{4.6}$$

Figure 4.10 displays the plots of $Y(s)$ for the three K values tested. With this information, the system transfer function was calculated as

$$G(s) = \frac{Y(s)}{X(s)}. \tag{4.7}$$

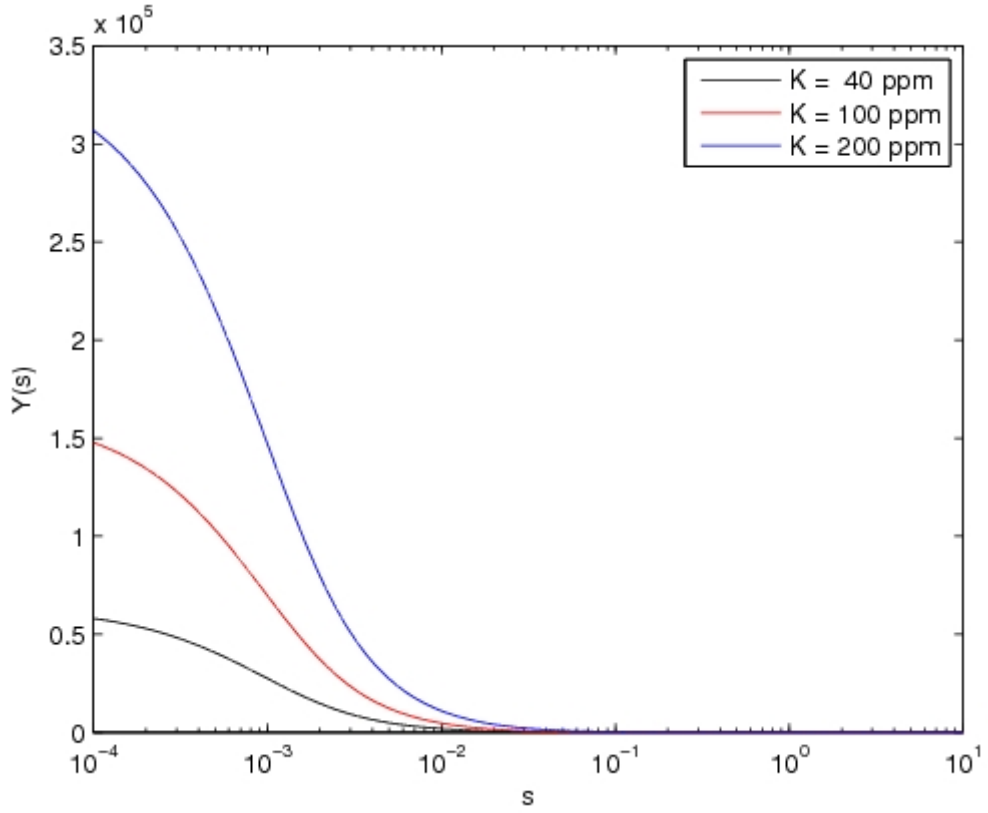

Figure 4.10. Laplace transform of $y(t)$.

The results are shown in Figure 4.11.

The three calculated transfer functions appear to have very similar trends, however, with noticeable differences in magnitude. If the system were truly linear, then the transfer function is expected to be independent of the supply concentration K. In other words, all of the curves in Figure 4.11 should overlie if the system was indeed linear. In order to determine if the observed differences in the three transfer functions were negligable, one of the transfer functions was used in conjunction with each of the measured $Y(s)$ to predict the corresponding input as follows

$$X(s) = \frac{Y(s)}{G(s)}. \tag{4.8}$$

Since $X(s) = K/s$, in this case, the supply concentration can be predicted as

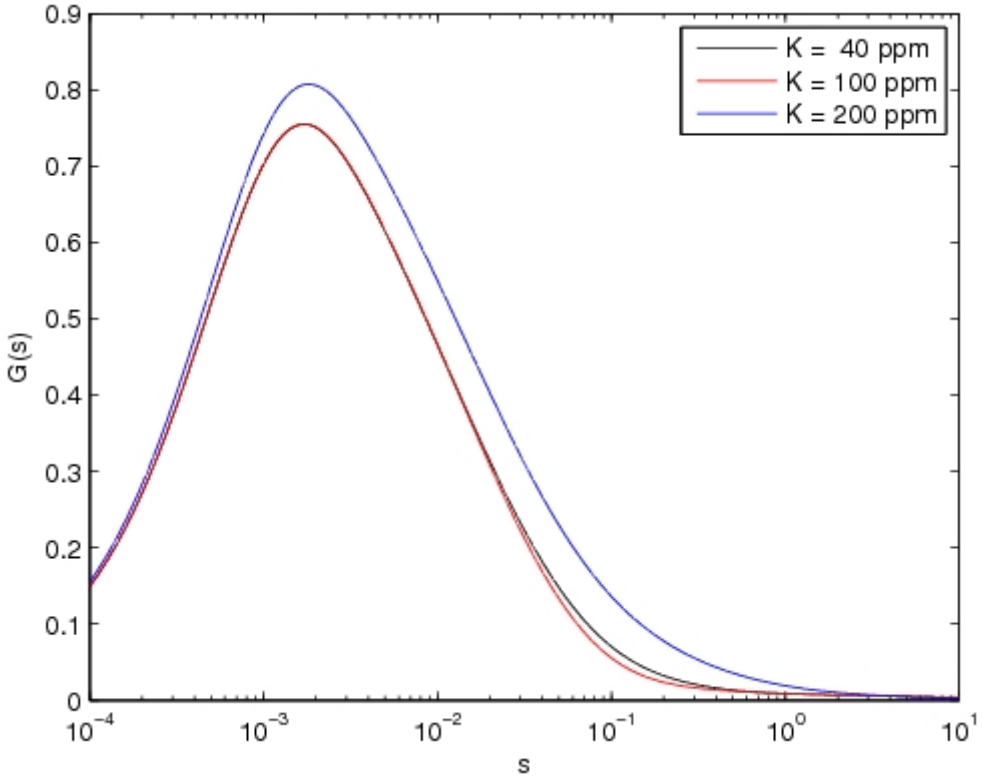

Figure 4.11. Resultant system transfer function calculated using the data in Figure 4.10.

$$\tilde{K} = \frac{s\,Y(s)}{G(s)}. \tag{4.9}$$

where ˜ has been used to denote the "predicted" value. Using the transfer function based on the 200 *ppm* supply, denoted as $G_{200}(s)$, one can predict the supply concentration for the two other tests, namely

$$\tilde{K}_{100} = \frac{s\,Y_{100}(s)}{G_{200}(s)}, \quad \tilde{K}_{40} = \frac{s\,Y_{40}(s)}{G_{200}(s)}. \tag{4.10}$$

Assuming the system is linear, and that $G_{200}(s)$ accurately reflects the true transfer function, then the $\tilde{K}$ values calculated from equation(4.10) should remain constant, i.e., $\tilde{K}_{100} = 100$ and $\tilde{K}_{40} = 40$, independent of s. The results of this prediction are compared in Figure 4.12 (solid lines) with the theory (dashed lines).

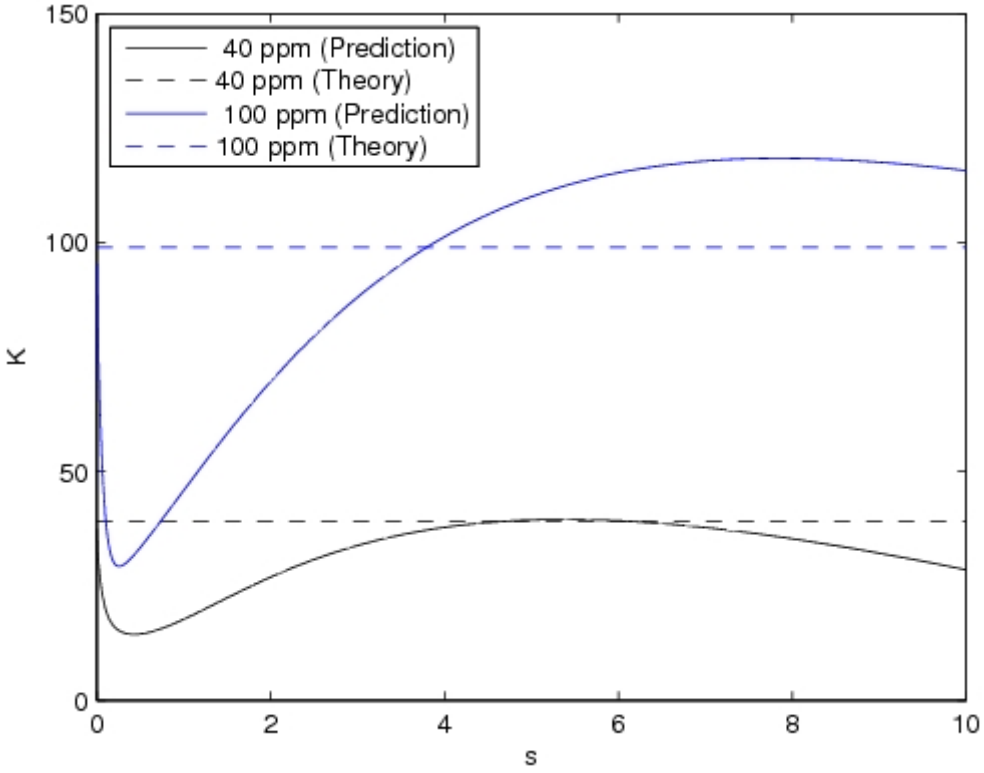

Figure 4.12. K prediction based the transfer function derived from the 200 *ppm* data.

Note, because of the manner in which $G_{200}(s)$ was calculated, $\tilde{K}_{200} = \frac{sY_{200}(s)}{G_{200}(s)}$ must identically be equal to 200. Therefore, this case is not shown in Figure 4.12.

As apparent, the transfer function derived from the 200 *ppm* test data fails to predict the correct supply concentration for the 40 *ppm* and 100 *ppm* tests. The same behavior was found when using the other transfer functions, $G_{40}(s)$ and $G_{100}(s)$. In conclusion, the present results indicate that the pollution measurement device cannot be modeled as a simple linear system which, therefore, precludes the use of equation (4.4) to determine time-resolved supply concentration. However, the response appears to be only slightly nonlinear. It is suggested that future work target this area to try to identify a suitable weakly nonlinear model.

4.2 Flight Test

A series of flight tests were conducted in order to verify that all of the chosen components would function together as designed in the actual aircraft. Due to the fact that the output from the pollution measurement device does not accurately reflect the CO concentration encountered, no attempt was made to prove the accuracy of the measurements. The following test results are presented to show that the pollution measurement device and custom control/interface circuit card communicate properly with the autopilot during flight.

A suitable testing location was identified with few obstructions, excellent visibility, and a low-traffic road for aircraft retrieval. The location used was McGregor Lane in Saratoga Springs, Utah. A map of the flight test area was uploaded to the Virtual Cockpit and was used to accurately select a take-off zone, waypoints, rally zone, and landing approach. Figure 4.13 shows the map with the flight plan settings as well as the actual path of the aircraft, as viewed in Virtual Cockpit.

During the flight, the autopilot precision data logger was used to record altitude, GPS position (latitude and longitude), barometric pressure, the microprocessor out-

Figure 4.13. Map of the flight path used flight testing as viewed in Virtual Cockpit. Distance between waypoints 1 and 2 is approximately 320 m.

put, CO sensor output, and temperature. Figure 4.14 shows the raw data collected during one of the test flights, as recorded by the autopilot for a sample period of 45 *sec*. The data in Figure 4.14 were collected as the aircraft navigated from waypoint 2 to waypoint 5 as shown in Figure 4.13. These data represent the raw output sent from the custom circuit card to the ADC on the autopilot and include the microprocessor, CO sensor, and thermocouple output voltages.

The microprocessor signal was used to identify the moment the valves opened or closed. When the linear actuator (used to open and close the valves) is stationary the microprocessor output voltage reads approximately 2.4 *volts*. While the actuator is in motion, the microprocessor output voltage drops to 0 *volts*. The drop in voltage represents the instant when the valves open or close. By noting the valve state prior to flight, it is possible to track the times when the valves are open versus closed. The CO sensor output represented the concentration of CO as measured by the CO sensor. Finally, the thermocouple output signal represented the temperature at each point as measured by the thermocouple.

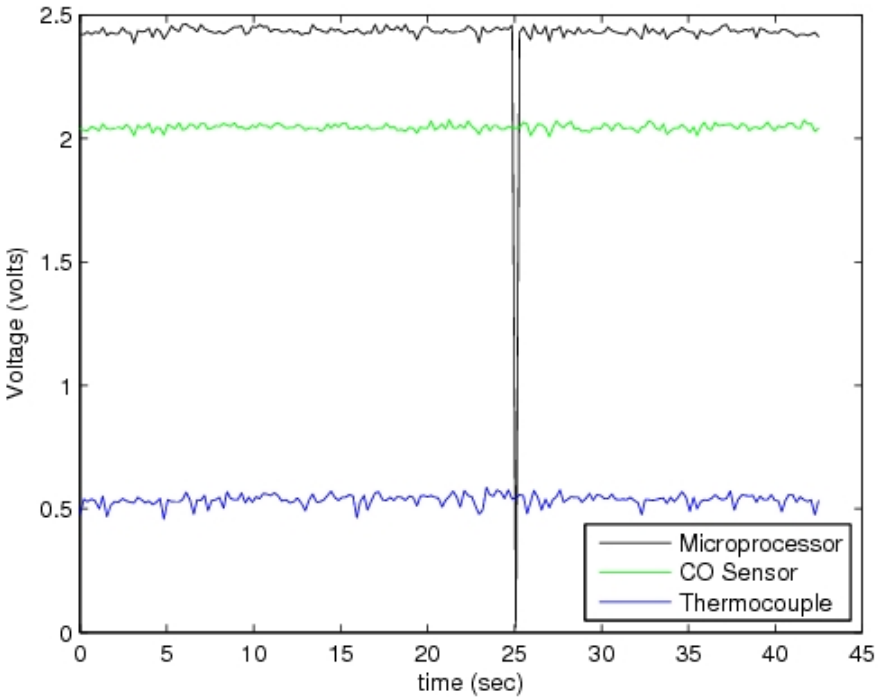

Figure 4.14. Raw data recorded during flight testing.

The CO sensor output voltage, V_{ADC}, as measured by the autopilot ADC was converted to the actual sensor output voltage, V_{sensor}, using

$$V_{sensor} = 2.5\,V_{ADC} - 5. \tag{4.11}$$

Due to the fact that the sensor was utilized in air with properties different from those that occurred during calibration, it was necessary to adjust V_{sensor} based on the local pressure and temperature. Figure 4.15 shows the actual CO concentration as calculated using equation (2.1).

Based on the experience from the flight test, it was verified that the custom circuit card, pollution measurement device, and CO sensor circuitry were functional and successfully able to communicate with each other as well as with the autopilot data acquisition system. The aircraft successfully followed the programmed flight plan and was able to record the desired data. Possible explanations for the rapid variation in CO concentration observed in Figure 4.15 include fluctuations in the CO

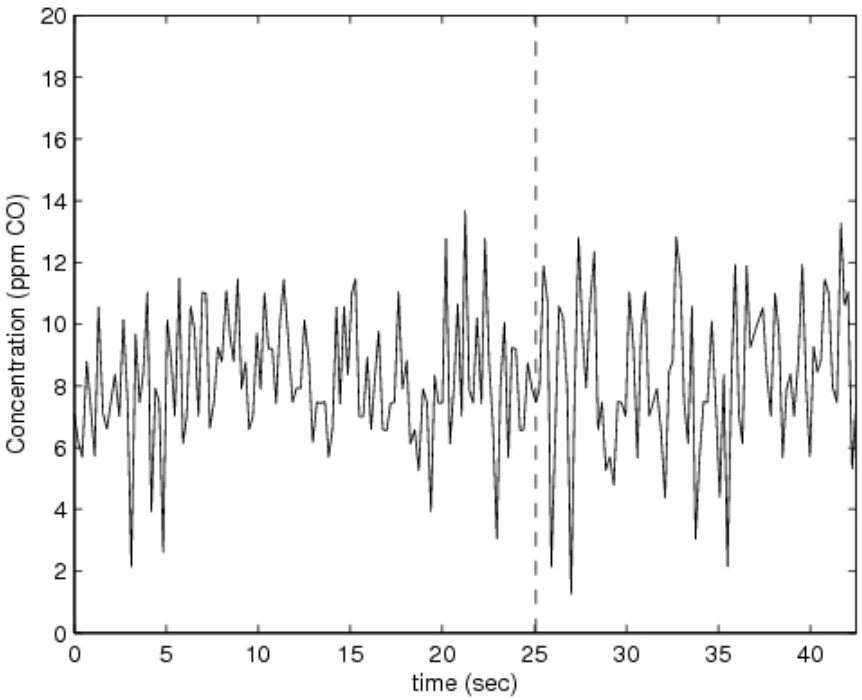

Figure 4.15. Actual CO concentration recorded during flight testing. The vertical dashed line indicates the instant of the valve closure.

levels intercepted during flight, interference to the sensor output signal by the RF transmitter, or the inherent uncertainty of the sensor. If the fluctuations were due to variations in the CO concentrations encountered during flight, the fluctuations would subside once the valves of the pollution measurement device were closed. As seen in Figure 4.15, fluctuations in the sensor output occurred both before and after the valves close. Therefore, it appears that the variation in the concentration was not due to fluctuations in the CO concentration, but was due to either RF interference or sensor uncertainty. Future work should be performed in order to identify the source of the fluctuations and to reduce their effects if possible.

CHAPTER 5

SUMMARY

The SAMI system provides a new method for monitoring air pollution levels in distant or hazardous areas. The SAMI system utilizes an aircraft outfitted with an autopilot system capable of autonomously flying the aircraft with a payload of pollution measurement equipment. The autopilot has the capability of recording a variety of variables such as GPS coordinates, altitude, and pressure, as well was three external analog signals.

The aircraft employs an innovative pollution measurement device. The device is capable of capturing static air samples and measuring the concentration of a specific gas in that sample. A set of valves, driven by a linear actuator and gear system, opens and closes at predetermined intervals, capturing the static air sample. A CO sensor mounted in the cavity where the air sample is captured is used to determine the concentration of the gas of interest in that sample. A custom circuit card was designed to operate the air sample capture device features, to operate the gas sensor, and to monitor the ambient air temperature. A connection between the autopilot and the custom circuit card allowed the autopilot to record important pollution measurement data such as valve position, sensor output, and ambient temperature.

Both wind tunnel testing and numerical simulations of the aircraft were conducted. The data from these tests were used to aid in the selection the inlet and outlet locations of the pollution measurement device. The pressure difference on the wing at the inlet and outlet locations was used to force air to flow through the pollution measurement device during flight, eliminating the need for an external pump. Through testing and analysis it was determined that when the pollution measurement device captures an air sample, the device consumes almost 42 % of the original CO

concentration. Unfortunately, this limited the usefulness of the data collected while the valves were closed.

The valves were tested and determined to properly seal the pollution measurement device. The response time of the system was determined in order to identify the time required for the sensor output to stabilize. The response time of the system was found to be as long as seven minutes, a relatively long time when attempting to gather data at as many locations as possible in a short amount of time. This response time was attributed to the filter built into this specific version of the sensor to block H_2S. Transfer functions for the system were also calculated; however, the system was determined to be nonlinear and, therefore, unable to be characterized using a single transfer function. Finally, flight testing with all of the components showed that the entire system worked together as designed.

5.1 Future Work

An increase in the internal volume of the pollution measurement device would reduce the effects of CO consumption during pollution data collection. Because the consumption rate of the pollution measurement device is inversely proportional to the internal volume of the device, an increase in the volume of air captured for sampling would reduce the percentage of CO consumed per sample. Table 5.1 demonstrates the effect of volume on the consumption rate, and therefore, the percentage of the captured sample consumed.

A larger pollution measurement device may necessitate a larger airframe. A

Table 5.1. Effect of increased volume on the pollution measurement device consumption rate.

Multiple of Original Volume	Volume ($\times 10^6\ m^3$)	Consumption Rate ($\times 10^3\ 1/s$)	Percentage CO Consumed
1×	1.5	8.9	41.2 %
5.1×	7.6	1.8	10 %
10.4×	15.6	0.9	5 %
26×	39	0.3	2 %
51×	76.5	0.2	1 %

custom aircraft, similar to the Unicorn, may be designed and easily manufactured using EPP foam. The increased load-carrying capacity of a slightly larger aircraft could warrant the inclusion of additional battery packs. Additional battery packs would increase to total flight time, and subsequently range, of the aircraft.

The custom circuitry may be improved in multiple ways. First, a custom printed circuit board (PCB) can easily be designed and manufactured for a relatively low cost because so few components are used. A PCB would also allow the majority of the components to be replaced by surface-mounted components (SMCs). SMCs generally have a low profile and their use would significantly reduce the overall thickness of the circuit card.

Further stabilization of the CO sensor output may be obtained by incorporating electromagnetic interference (EMI) shielding. EMI could easily be caused by the RF signals introduced by the communication between the SAMI aircraft and the ground station as well as by a variety of external sources. Depending on the location of the flight, a number of electromagnetic sources may interfere with the function of the gas sensor and associated circuitry. The effects of EMI on the sensor output should be tested and sufficient EMI shielding should be included in subsequent designs.

Finally, the response time of the pollution measurement device could be reduced significantly by utilizing the nonfiltered version of the CO sensor. The filter is intended to prevent H_2S from reacting with the sensor. However, the filter also increases the response time of the sensor. Research could be conducted to identify the expected levels of H_2S the pollution measurement device may encounter. If the risk of encountering H_2S is determined to be negligible, the nonfiltered sensor may be used and the system response time shortened.

APPENDIX A

DERIVATION OF DESIGN EQUATIONS

In order to predict the airflow through the pollution measurement device a mathematical model was derived. This derivation is presented first. Next, the derivation of the equation used to determine the wind tunnel velocity is presented.

A.1 Mathematical Flow Model

This mathematical model was derived to model the airflow through the pollution measurement device. The original governing equation is (Fox *et al.*, 2004),

$$\left(\frac{P_1}{\rho} + \alpha_1 \frac{\bar{V}_1^2}{2} + g\, z_1\right) - \left(\frac{P_2}{\rho} + \alpha_2 \frac{\bar{V}_2^2}{2} + g\, z_2\right) = h_{l_T}, \tag{A.1}$$

where P denotes the pressure of the air, ρ denotes the density of the air, α is the kinetic energy coefficient, V is the average velocity of the air, g is the acceleration of gravity, z is the height and h_{l_T} is total head loss. The subscripts 1 and 2 denote locations in the flow where the pressure, density, kinetic energy coefficient, velocity and height are considered. Subscript 1 corresponds to the device inlet location and subscript 2 corresponds to the device outlet location. In this application, the cross-sectional geometry of the tube through the device remains relatively constant and thus $\bar{V}_1 = \bar{V}_2$. Also, the change in height, Δz, is negligible and results in $z_1 = z_2$. Finally, according to Fox *et al.* (2004) α is very close to unity for applications with high Reynold's numbers. Applying these assumptions reduces equation (A.1) to

$$\left(\frac{P_1 - P_2}{\rho}\right) = h_{l_T}. \tag{A.2}$$

Fox *et al.* (2004) also states that the total head loss, h_{l_T}, is the sum of the major losses, h_l, and the minor losses, h_{l_m}. Major losses are pressure losses due to friction between the air and the pipe walls. Minor losses are due to changes in geometry such as entrances and fittings. Applying this information to equation (A.2) results in,

$$\left(\frac{P_1 - P_2}{\rho}\right) = h_l + h_{l_m}. \tag{A.3}$$

Fox *et al.* (2004) defined the major losses in a pipe as

$$h_l = f\,\frac{L}{D}\,\frac{\bar{V}^2}{2}, \tag{A.4}$$

where f is the friction factor, L is the length of the pipe and D is the inside diameter of the pipe. The minor losses as

$$h_{l_m} = K_l\,\frac{\bar{V}^2}{2}, \tag{A.5}$$

where K_l is the loss coefficient. The only minor loss of note occurs at the tube entrance. According to Fox *et al.* (2004) for a square-edged entrance $K_l = 0.5$. Equation (A.5) becomes

$$h_{l_m} = 0.5\,\frac{\bar{V}^2}{2}. \tag{A.6}$$

Substituting equations (A.4) and (A.6) into equation (A.3) with simplification yields

$$\left(\frac{P_1 - P_2}{\rho}\right) = \left(f\,\frac{L}{D} + 0.5\right)\,\frac{\bar{V}^2}{2}. \tag{A.7}$$

Equation (A.7) is rearranged such that all terms are on one side of the equation:

$$0 = \left(\frac{P_1 - P_2}{\rho}\right) - \left(f\,\frac{L}{D} + 0.5\right)\,\frac{\bar{V}^2}{2}. \tag{A.8}$$

The Colebrook formula is a very common numerical approximation for the friction factor, f, and is defined as (Fox *et al.*, 2004)

$$\frac{1}{f^{0.5}} = -2.0 \log\left(\frac{e/D}{3.7} + \frac{2.51}{Re\, f^{0.5}}\right). \tag{A.9}$$

Equation (A.9) is generally solved be selecting an initial guess and iterating. However, is has been found that using

$$f_0 = 0.25 \left[\log\left(\frac{e/D}{3.7} + \frac{5.74}{Re^{0.9}}\right)\right]^{-2} \tag{A.10}$$

as the initial guess causes equation (A.9) to converge within 1 percent of the actual solution in only one iteration (Fox *et al.*, 2004). Therefore, rearranging equation (A.9) yields

$$f = \sqrt[0.5]{\frac{1}{-2.0 \log\left(\frac{e/D}{3.7} + \frac{2.51}{Re\, f_0^{0.5}}\right)}} \tag{A.11}$$

where f_0 is found using equation (A.10).

Substituting equation (A.11) into equation (A.8)

$$0 = \left(\frac{P_1 - P_2}{\rho}\right) - \left(\left[\sqrt[0.5]{\frac{1}{-2.0 \log\left(\frac{e/D}{3.7} + \frac{2.51}{Re\, f_0^{0.5}}\right)}}\right] \frac{L}{D} + 0.5\right) \frac{\bar{V}^2}{2}. \tag{A.12}$$

Fox *et al.* (2004) defines the Reynold's number as

$$Re = \frac{\rho \bar{V}\, D}{\mu} \tag{A.13}$$

where μ is the dynamic viscosity of the air. Substituting equation (A.13) into equations (A.10) and (A.12) yields

$$f_0 = 0.25 \left(\log \left[\frac{e/D}{3.7} + \frac{5.74}{\left(\frac{\rho \bar{V} D}{\mu} \right)^{0.9}} \right] \right)^{-2} \tag{A.14}$$

and

$$0 = \left(\frac{P_1 - P_2}{\rho} \right) - \left[\left(\sqrt[0.5]{\frac{1}{-2.0 \log \left[\frac{e/D}{3.7} + \frac{2.51}{\left(\frac{\rho \bar{V} D}{\mu} \right) f_0^{0.5}} \right]}} \right) \frac{L}{D} + 0.5 \right] \frac{\bar{V}^2}{2} \tag{A.15}$$

respectively.

A.2 Wind Tunnel Velocity Equation

Because the flow in the wind tunnel is considered steady, incompressible, frictionless, along streamlines and because the density of the air is considered constant, the Bernoulli equation can be used to determine the velocity of the air. The Bernoulli equation is (Fox *et al.*, 2004)

$$\frac{p}{\rho} + \frac{V^2}{2} + g\, z = constant, \tag{A.16}$$

where p is the pressure, ρ is the density of the fluid, V is the velocity of the flow, g is the acceleration of gravity, and z is the height of the measurement point.

A pitot-static tube was used to determine the velocity of the air in the wind tunnel. A pitot-static tube measures difference between the stagnation and static pressures. The fluid pressure, velocity, and height at the static tap is denoted as p, V, and z respectively. At the stagnation tap the fluid pressure, velocity, and height are denoted as p_0, V_0, and z_0, respectively. Comparing the properties at both of the locations results in

$$\frac{p_0}{\rho} + \frac{{V_0}^2}{2} + g\, z_0 = \frac{p}{\rho} + \frac{V^2}{2} + g\, z \tag{A.17}$$

The change in height between the stagnation and static pressure taps on the pitot tube is negligible, therefore $z = z_0$. Also, according to the definition of stagnation the velocity of the fluid at the stagnation tap, V_0 is zero. Based on these conditions equation (A.16) can be reduced to

$$\frac{p_0}{\rho} = \frac{p}{\rho} + \frac{V^2}{2}. \tag{A.18}$$

Solving equation (A.18) for velocity

$$V = \sqrt{\frac{2\,(p_0 - p)}{\rho}}. \tag{A.19}$$

Because the wind tunnel testing was performed using air the density in equation (A.19) is that of air. Therefore, in this case $\rho = \rho_{air}$. Fox *et al.* (2004) also states that

$$p_0 - p = \rho_{Hg}\, g\, h_{Hg} \tag{A.20}$$

where ρ_{Hg} is the density of mercury and h_{Hg} is the measurement height of the mercury. This is appropriate as the measurements obtained were in mm Hg. In general it is easier to obtain density values of water at various temperatures rather than for mercury. The relationship between the densities of water and mercury is

$$\frac{\rho_{Hg}}{\rho_{H_2O}} = SG_{Hg} \tag{A.21}$$

where ρ_{H_2O} is the density of water and SG_{Hg} is the specific gravity of mercury. According to Fox *et al.* (2004) the specific gravity of mercury is 13.6. Solving equation (A.22) for the density of mercury and substituting in the value for the specific gravity of mercury we obtain

$$\rho_{Hg} = 13.6\,\rho_{H_2O} \tag{A.22}$$

Substituting equation (A.22) into equation (A.20) we obtain

$$p_0 - p = 13.6\,\rho_{H_2O}\,g\,h_{Hg}. \tag{A.23}$$

Equation (A.23) can now be substituted into equation (A.19),

$$V = \sqrt{\frac{2\,(13.6\,\rho_{H_2O}\,g\,h_{Hg})}{\rho_{air}}}. \tag{A.24}$$

APPENDIX B

BUCKINGHAM PI ANALYSIS

A Buckingham Pi analysis was done to correlate the results obtained during the wind tunnel testing using a scaled model to the full scale aircraft. The steps outlined by Fox *et al.* (2004) were followed in determining the Π groups.

First, the dimensional parameters involved were listed. The dimensional parameters chosen were the change in pressure ΔP, fluid density ρ, fluid dynamic viscosity μ, chord length c, and velocity V. Second, a set of primary dimensions was identified. Those primary dimensions were M for mass, L for length, and t for time. Next, all of the chosen parameters were listed in terms of the primary dimensions:

ΔP	ρ	μ	c	V
$\frac{M}{t^2\,L}$	$\frac{M}{L^3}$	$\frac{M}{L\,t}$	L	$\frac{L}{t}$

Fourth, the repeating parameters were chosen. In this case ρ, V, and c were chosen. To determine the number of resulting dimensionless Π groups the number of repeating parameters were subtracted from the number of dimensional parameters. Thus, two Π groups will be determined. The first Π group is

$$\Pi_1 = \rho^a\, V^b\, c^c\, \Delta P. \tag{B.1}$$

Next, the primary dimensions for each parameter are substituted into equation(B.1) and the right hand side of equation(B.1) is set equal to one in terms of M, L, and t.

$$\left(\frac{M}{L^3}\right)^a \left(\frac{L}{t}\right)^b (L)^c \left(\frac{M}{t^2\,L}\right) = M^0 L^0 t^0 \tag{B.2}$$

The exponents of M, L, and t were equated:

$$\begin{array}{rcl} M\text{:} & a+1=0 & a=-1 \\ L\text{:} & -3\,a+b+c-1=0 & c=0 \\ t\text{:} & -b-2=0 & b=-2 \end{array}$$

Therefore,

$$\Pi_1 = \frac{\Delta P}{\rho\, V^2}. \tag{B.3}$$

Equation(B.3) is the *Euler number* which is also known as the *pressure coefficient*, C_p. The denominator is also multiplied by $1/2$ such that the denominator represents the dynamic pressure. Thus

$$C_P = \frac{\Delta P}{\frac{1}{2}\rho\, V^2}. \tag{B.4}$$

Similarly, the second Π group is

$$\Pi_2 = \rho^a\, V^b\, c^c\, \mu. \tag{B.5}$$

The primary dimensions for each parameter are again substituted into equation(B.5) and the right hand side of equation(B.1) is set equal to one in terms of M, L, and t.

$$\left(\frac{M}{L^3}\right)^a \left(\frac{L}{t}\right)^b (L)^c \left(\frac{M}{L\,t}\right) = M^0 L^0 t^0 \tag{B.6}$$

The exponents of M, L, and t were equated:

$$\begin{array}{rcl} M\text{:} & a+1=0 & a=-1 \\ L\text{:} & -3\,a+b+c-1=0 & c=-1 \\ t\text{:} & -b-1=0 & b=-1 \end{array}$$

Therefore,

$$\Pi_2 = \frac{\mu}{\rho V c}. \tag{B.7}$$

Equation(B.7) is the inverse of the *Reynolds number*, Re which is defined as

$$Re = \frac{\rho V c}{\mu}. \tag{B.8}$$

Next, both groups are checked to verify that each is truly dimensionless.

$$[\Pi_1] = \left[\frac{\Delta P}{\rho V^2}\right] \longrightarrow \frac{M}{t^2 L}\,\frac{L^3}{M}\,\frac{t^2}{L^2} = 1$$

$$[\Pi_2] = \left[\frac{\mu}{\rho V c}\right] \longrightarrow \frac{M}{L t}\,\frac{L^3}{M}\,\frac{t}{L}\frac{1}{L} = 1.$$

As shown above, both Π groups are indeed dimensionless. Finally, the functional relationship between the Π groups is

$$\Pi_1 = f(\Pi_2) \tag{B.9}$$

or

$$\frac{\Delta P}{\rho V^2} = f\left(\frac{\mu}{\rho V c}\right) \tag{B.10}$$

or

$$C_p = f(Re). \tag{B.11}$$

APPENDIX C

CO SENSOR CONSUMPTION RATE DERIVATION

The manufacturer specifies that the present sensor produces $70 \pm 15\ nA/ppm\,CO$, denoted as R_{CP}, or the current production rate. Using the given sensor current production rate, along with the fact that two electrons are released for each CO molecule consumed, the sensor consumption rate, R_{SC} $(mol\ \ CO/ppm \cdot S)$, was determined using

$$R_{SC} = \frac{R_{CP}\ \left(10^{-9}\ \frac{A}{nA}\right)\ \left(1\ \frac{C}{A \cdot s}\right)}{\left(2\ \frac{e}{molecule\,CO}\right)\ \left(1.602 \times 10^{-19}\ \frac{C}{e}\right)\ \left(6.022 \times 10^{23}\ \frac{molecules\,CO}{mol\,CO}\right)} \tag{C.1}$$

The pollution measurement device consumption rate, r $(1/s)$, was defined as

$$r = \left(\frac{R_{SC}\ (10^6\,ppm)}{Vol\,c_a}\right) \tag{C.2}$$

where Vol (m^3) is defined as the internal volume enclosed within the pollution measurement device and c_a $(mol\ CO/m^3)$, the molar concentration of air, is defined as

$$c_a = \frac{P}{R^* T} \tag{C.3}$$

where P is the local atmospheric pressure in Pa, R^* is the universal gas constant $(8.32\ J/mol \cdot K)$, and T is the local absolute temperature in K (Arya, 1999). Using the expected sensor current production rate range the measurement device consumption rate range was determined to be 5.3×10^{-3} to $8.2 \times 10^{-3}\ 1/s$.

APPENDIX D

CO SENSOR DATA SHEET

(See Supplementary Material)

REFERENCES

2008 Electrochemical sensor operation and performance notes. *Tech. Rep.* APP Note EC-0108-1. KWJ Engineering Inc, Newark, CA.

2010 *FullCure Materials*. Billerica, Massachusetts.

2011 Ambient air quality monitoring program - pollutants of concern.

2011 Emissions limits database.

2011 National Ambient Air Quality Standards (NAAQS).

Arya, S. P. 1999 *Air Pollution Meteorology and Dispersion*. New York, NY: Oxford University Press.

Bartholmai, M. & Neumann, P. 2010 Micro-drone for gas measurement in hazardous scenarios via remote sensing. *Tech. Rep.* ISSN: 1792-5088. German Federal Institue for Materials Research and Testing and AirRobot GmbH & Co. KG.

Corrigan, C., Roberts, G., Ramana, M., Kim, D. & Ramanathan, V. 2008 Capturing vertical profiles of aerosols and black carbon over the Indian Ocean using autonomous unmanned aerial vehicles. *Atmospheric Chemistry and Physics* **8** (3), 737–747.

Everaerts, J., Lewyckyj, N. & Fransaer, D. 2004 Pegasus: Design of a stratospheric long endurance UAV system for remote sensing. In *Altan, O.(ed): Proceedings of the 20th ISPRS Congress, Istanbul 2004, IAPRS*, pp. 29–33. Vito, Flemish Institute for Technological Research, Belgium.

Fox, R., McDonald, A. & Pritchard, P. 2004 *Introduction to Fluid Mechanics*, 6th edn. New York, NY: John Wiley and Sons.

Franklin, G. F., Powell, J. D. & Emami-Naeini, A. 2002 *Feedback Control of Dynamic Systems*, 4th edn. Upper Saddle River, New Jersey: Prentice-Hall, Inc.

Holland, G., Webster, P., Curry, J., Tyrell, G., Gauntlett, D., Brett, G., Becker, J., Hoag, R. & Vaglienti, W. 2001 The Aerosonde robotic aircraft: A new paradigm for environmental observations. *American Meteorological Society* **82** (5), 889–901.

Klingenberg, H. H., Fix, A., Mahnke, P. & Lemmerz, C. 2007 Mobile remote detection device and remote detection method for methane gas accumulations. *Tech. Rep.* U.S. patent no. 7312452. Deutches Zentrum fur Luft- und Raumfahrt E. V., Bonn, Denmark.

Logothetis, E. M. & Soltis, R. E. 1993 Apparatus for sensing hydrocarbons and carbon monoxide. *Tech. Rep.* U.S. patent no. 5250169. Ford Motor Company, Dearborn, MI.

Patel, V. 2011 Personal Communication.

Patterson, M., Mulligan, A., Douglas, J., Robinson, J., Wardell, L. & Pallister, J. 2005 Volcano surveillance by ACR silver fox. *Tech. Rep.* AIAA Paper 2005 - 6954. Advanced Ceramics Research and USGS Cascades Volcano Observatory.

Prasad, C. R., Lin, B. & Lee, H. S. 2011 Airborne tunable mid-ir laser gas-correlation sensor. *Tech. Rep.* U.S. patent no. 7884937. Science & Engineering Services, Inc., Columbia, MD.

Spalart, P. & Allmaras, S. 1992 A one-equation turbulence model for aerodynamic flows. *Tech. Rep.* AIAA Paper 92–0439. American Institute of Aeronautics and Astronautics.

Spoerry, T. & Wong, K. 2001 Design and development of a micro air vehicle (μav) concept: Project Bidule. In *The 9th Annual International Aerospace Congress*. School of Aerospace, Mechanical and Mechatronic Engineering, University of Sydney, NSW, Australia.

Vij, A. K. 2010 Sensing system and components for detecting and remotely monitoring carbon monoxide in a space of concern. *Tech. Rep.* U.S. patent no. 7746240. CO Guardian LLC, Tucson, AZ.

Wilcox, D. C. 2006 *Turbulence Modeling for CFD*, 3rd edn. La Canada, California: DCW Industries, Inc.

Wong, K. C. 2001 UAV design activities in a university environment. In *The 9th Annual International Aerospace Congress*. School of Aerospace, Mechanical and Mechatronic Engineering, University of Sydney, NSW, Australia.

Yufa, A. L. 2009 Method and particle measuring and counting apparatus with selectable channels of a specimen flow. *Tech. Rep.* U.S. patent no. 7573573. Colton, CA.

Transducer Technology Division

8440 Central Ave, Suite# 2C, Newark, CA-94560
510-791-0951 support@transducertech.com

INNOVATIVE SENSORS.
CREATIVE SOLUTIONS

3 Electrode T1 Series Carbon Monoxide Sensor – 3ET1CO1500

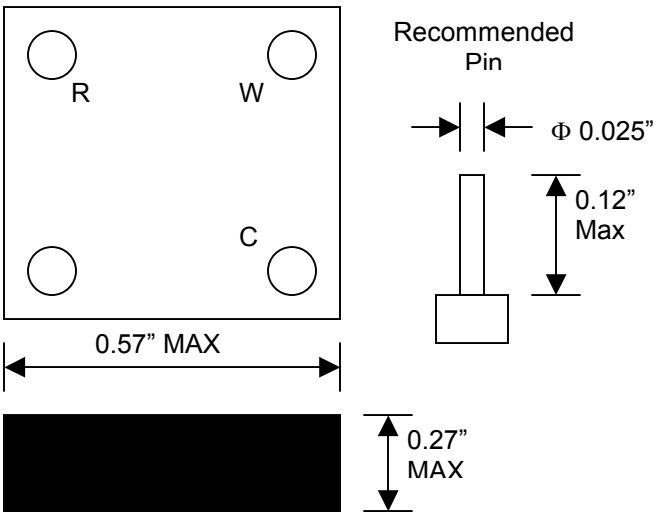

Mechanical Specifications	
Dimensions	0.57” X 0.57” X 0.27”.
Weight	Less than 2 gram
Material	Polypropylene
Electrolyte	Etching liquid in matrix
Connections	Socket
Gas Supply	Diffusion through porous membrane

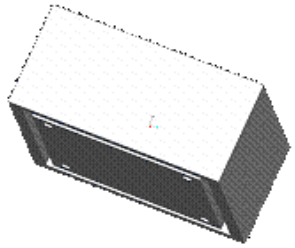

	3ET1CO1500
Measuring range	0-500 PPM
Maximum overload	1500 PPM
Measuring Principle	Electrochemical Oxidation of CO
Working Electrode Potential	Not required
Output Signal, Zero, 25 °C	< ± 5 ppm equivalent maximum
Output Signal, Span, 25 °C	70 to ± 15 nA / PPM
Lower Detection Limit	< 0.5 PPM (depends on circuitry)
Resolution	± 0.5 PPM (depends on circuitry)
Zero Reproducibility	± 2% of reading or 2 ppm
Span Reproducibility	± 1% of reading or 1 ppm
Output Linearity	Linear
Response Time (t-90)	< 30s typical at 20° C
Stabilization time	15 minutes (first installed in a circuit) thereafter < 30 sec.
Long Term Drift – Zero	Zero Signal ≤ ± 2 PPM / month
Long Term Drift – Span	Output Signal ≤ ± 2% of reading per month
Maximum Zero Shift	< 8 ppm equivalent (-20°C to +40°C)
Operating Temperature	-20 to 50° C (0 – 35°C recommended)
Operating Pressure Range	± 0.2 atm (recommended)
Operating Humidity Range	15 to 90% RH
Estimated Service Life	> 2 Years
Storage Temperature	22° C Recommended
Storage Pressure	1 ± 0.2 atm Recommended
Storage Humidity Range	50 to 65% RH Recommended
Storage Life	1 year in sealed package
Warranty	One year (extended warranty available)

Contact TTI for application information. TTI reserves the right to alter design features and specifications without notice.